## Abbreviations

DC      Direct Current
D-Gun      Detonation Gun
FTIR      Fourier Transform Infra-Red
GLR      Gas-to-Liquid mass Ratio
HVAF      High Velocity Air Fuel
HVOF      High Velocity Oxygen Fuel
i.d.      internal diameter
ICP      Inductively Coupled Plasma
LTE      Local Thermodynamic Equilibrium
PIV      Particle Image Velocimetry
RF      Radio Frequency
SHS      Self-propagation High temperature Synthesis
XRD      X-Ray Diffraction
YSZ      Yittria Stabilized Zirconia

## 4.1 Introduction

Thermal spray coatings technology is essentially based on the in-flight heating, melting and atomization of the material to be used for the coating followed by the deposition of the formed molten droplets on the substrates as successive splats, which pile up forming the coating. A combustion flame or an electrical discharge is used as the heating medium in which the coating material is injected in the form of powder, wire, solution, or liquid suspension. Since the coating material is in contact with the heating medium for less than a few milliseconds, the proper control of the trajectories of the particles or droplets and their temperature history is of critical importance for the overall success of the operation. A slight deviation from near-optimal conditions can easily lead to poor results due to either the lack of melting of particles, insufficient impact velocities, or the modification of their chemical composition due to inflight particle evaporation or unwanted chemical reactions.

This chapter is mainly devoted to a review of the different fundamental phenomena governing the inflight interaction between the coating material and the heating medium during their short contact time. Comprehensive studies on the subject were reported in the eighties and nineties by Boulos (1976)(1978)(1985), Mostaghimi J et al. (1984)(1987)(1989), Proulx P et al. (1985)(1987)(1990)(1991)a,b, Vardelle M et al. (1983)(1988), Bourdin et al. (1993), Fauchais et al. (1997)a,b, Chen and Pfender (1982a, b), Pfender E. (1985) (1989) (1999), Pfender et al. (1985, 1998), Boulos et al (2004)(2016) and Xue S et al. (2001)(2019). Studies and developments were also published for cold spray, HVOF, and D-gun and more recently for suspension and solution plasma spraying. Following a brief introduction of the properties of particles and powders, the basic phenomena governing the momentum and heat transfer between a single spherical particle and a high-energy gas flow is discussed. This includes such phenomena as plasma-particle momentum and heat transfer, transient heating, melting and evaporation of particles under plasma conditions, mass transfer and chemical reactions for liquid or gaseous phases. Particle trajectory and temperature history calculations are discussed next for ensemble of particles/powder injected into the plasma flow under dilute loading condition, which is limited to situations where the mass feed rate of particles/powder in the flow is sufficiently low so as not to have any impact on the plasma flow and temperature fields. This is followed by a discussion of the treatment of ensembles of particles/powder in gas flows including particle injection techniques and thermal loading effects resulting from plasma–particle interactions under dense loading conditions, which is of critical importance in any realistic discussion of the inflight transient heating and melting of the particles.

## 4.2  Overview of Powder Characteristics

Powders are by definition composed of individual particles, which can be of different sizes, shapes and compositions. Their properties are closely dependent on their manufacturing technique and the thermophysical properties of the material. Particles are generally characterized by the following:

- Individual particle diameter and morphology, including their shape, sphericity, and porosity
- Particle chemical composition and crystal structure

Powders on the other hand are characterized by the following:

- Particle size distribution, mean particle diameter, and standard deviation
- Apparent density and tap-density of the powder, the latter corresponding to the highest packing density of the powder
- Powder flowability (e.g., Hall-flow) reflecting its ability to free flowing
- Angle of internal friction and angle of repose, both of which relate to properties of the packed powder
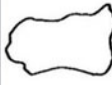
## 4.2.1  Individual Particle Size and Morphology

Powders used in thermal spray operating are composed of ensembles of particles, which can have a wide range of shapes and properties depending on their manufacturing technique. Typical examples of thermal spray powders are given in Fig. 4.1. These include the following:

(a) Water-atomized iron powder (Fe-C-Si) with a bulky rounded edged form (Tsunekawa et al. 2006)
(b) Sintered and crushed tungsten carbide powder (WC-Co-Cr) which gives rise to bulky, porous, round edged particles [*Starck Amperit 553.065*].
(c) Fused and crushed alumina powder ($Al_2O_3$) with its sharp-edged fully dense particles (Laha et al. (2005).
(d) Bulk molybdenum disulfide powder ($MoS_2$) with their natural flaky structure
(e) Plasma spheroidized molybdenum powder (Mo) with its generally perfect spherical dense particles (Boulos 2016)
(f) Plasma atomized titanium alloy powder (Ti-6Al-4V) showing a dense spherical morphology (Polak et al 2017)

It may be noted that the production of dense spherical metallic powders is generally limited to plasma spheroidized
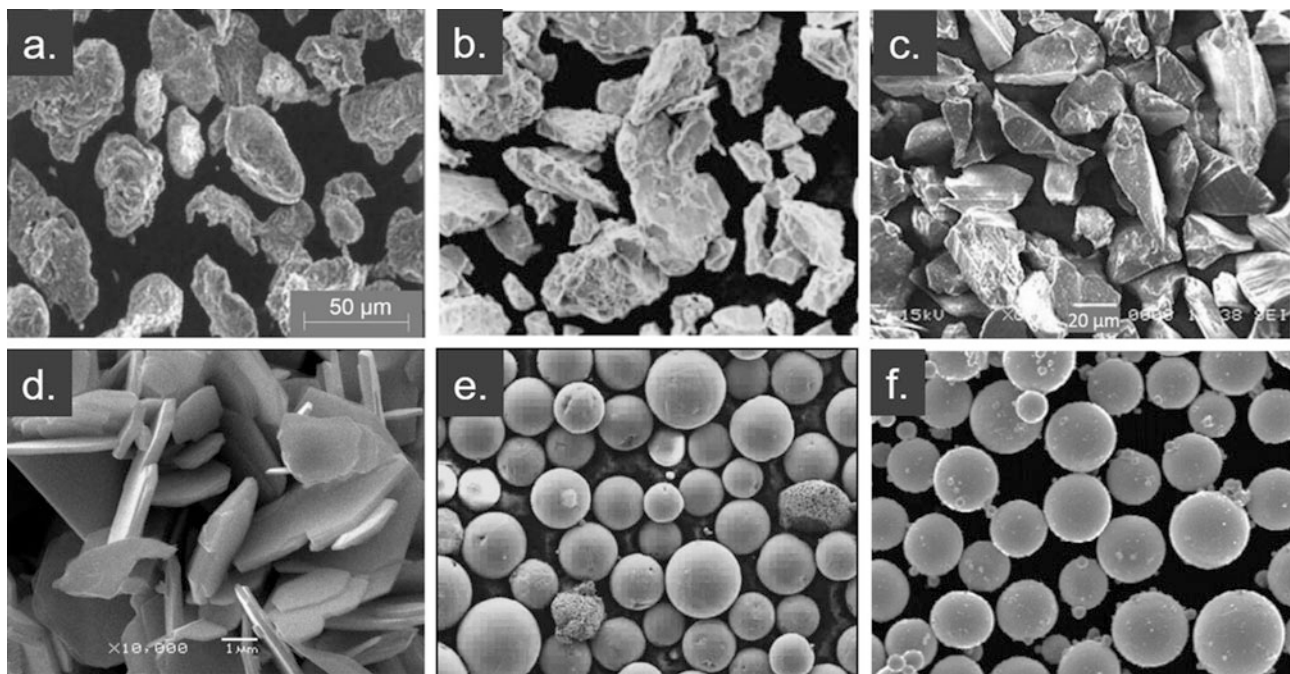


**Fig. 4.1** Examples of plasma-spray powder particles reflecting different manufacturing routes

| Powder type Manufacturer | Fused and milled | Sintered and milled | Agglomerated and sintered | Spheroidized | Atomized |
|---|---|---|---|---|---|
| | | | | | |
| **Particle shape** | Blocky - angular | Blocky - angular | Spherical | Spherical | Spherical - irregular |
| **Porosity** | Dense | Dense - porous | Porous | Dense - hollow | Porous - hollow |
| **Crystalline size** | Course-fine | Course - fine | Medium - fine | Medium - fine | Fine |
| **Homogeneity** | Alloyed | Alloyed | Alloyed - heterogeneous | Alloyed - heterogeneous | Alloyed |

**Fig. 4.2** Specific YSZ ($ZrO_2$–8 wt.% $Y_2O_3$) powder characteristics depending on their manufacturing route, Schwier (1986)
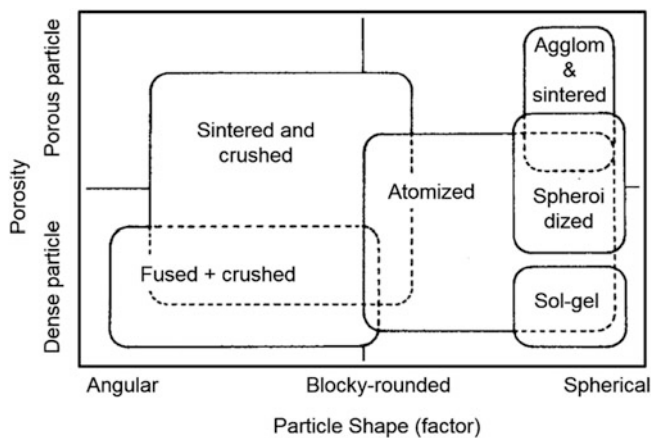


**Fig. 4.3** Powder characteristics, porosity, and particle shape, as a function of their manufacturing process, Schwier (1986)
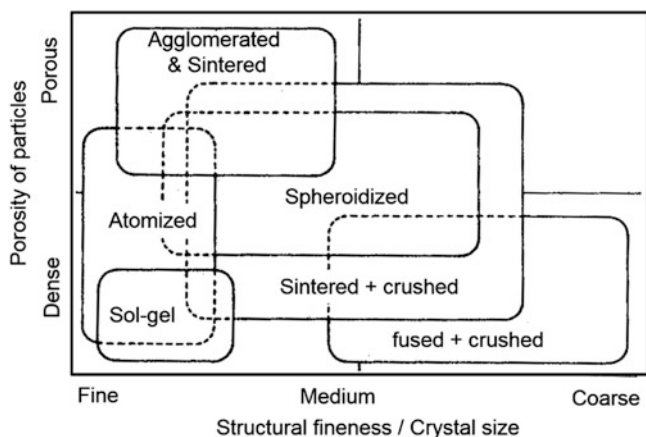


**Fig. 4.4** Powder characteristics—porosity and structural fineness—as a function of their manufacturing process, Schwier (1986)

or plasma atomized powders, Fig. 4.1e, f, which are formed in the molten state and acquire their spherical shape through surface tension effect. A study of the link between the powder manufacturing technique and the morphology of the particles obtained for Yttria-stabilized Zirconia (8 wt.% $Y_2O_3$) was reported by Schwier (1986). The results given in Figs. 4.2, 4.3 and 4.4 show agglomerated and sintered powders commonly used in plasma spray coating tend to be composed of porous particles with a rounded shape and a rather fine crystal structure. Fused and crushed powders, are on the other hand, are composed of blocky and dense particles with sharp edges, and medium to coarse gain structure.

A systematic effort has been devoted in literature in order to develop appropriate parameters to characterize the different particle morphologies. According to Reist (1993), particles with a bulky shape, whether rounded or sharp edged, can be described by an equivalent particle diameter and a shape factor, such as "sphericity." The Feret's diameter and the Martin's diameter, illustrated in Fig. 4.5, are commonly used based on the image analysis of projected particle micrographs. The *Feret's* diameter is defined as the maximum distance from edge to edge of each particle in the image along an arbitrary but fixed axis applicable to all particle. The *Martin's* diameter, on the other hand, is the length of the line that separates each particle into two equal surfaces. Reist (1993) points out that since these measurements can vary depending on the orientation of the particle, they are only valid if averaged over a number of particles and if all measurements are made parallel to one another.

Alternately the following definitions of an equivalent particle diameter are commonly used, such as:
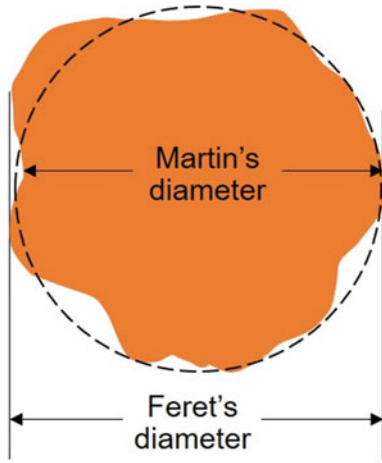
**Fig. 4.5** Illustration of Feret's and Martin's diameters, Reist (1993)

**Equivalent perimeter diameter,** $d_{pp}$, is defined as the diameter of the circle, which has the same perimeter as that of the projected particle image:

$$d_{pp} = \frac{P_p}{\pi} \qquad (4.1)$$

where $P_p$ is the perimeter of the projected image of the particle.

**Equivalent projected area diameter**, $d_{pa}$, is defined as the diameter of the circle having the same projected surface area as that of the particle.

$$d_{pa} = \sqrt{\frac{4a_p}{\pi}} \qquad (4.2)$$

where $a_p$ is the projected surface area of the particle.

**Equivalent volume diameter**, $d_{pv}$, is defined as the diameter of the sphere having the same volume as that of the particle.

$$d_{pv} = \left(\frac{6V_p}{\pi}\right)^{\frac{1}{3}} \qquad (4.3)$$

where $V_p$ is the volume of the particle.

The projected area diameter, and the equivalent volume diameter, are often combined with secondary parameter, which reflects how close are the particle's from being a sphere. These are defined as "**Circularity"** and "**Sphericity**." The circularity "$C$" is defined as the ratio of the perimeter of the circle with the same projected surface area of the particle, $\pi\, d_{pa}$, to that of the actual projected image of the particle, $P_p$.

$$C = \frac{\pi\, d_{pa}}{P_p} \qquad (4.4)$$

The **sphericity**, $\psi$ on the other hand is defined as the ratio of the surface area of the sphere of equal volume as the particle to the surface area of the particle.

$$\psi = \frac{\pi d_{pv}^2}{A_p} \qquad (4.5)$$

Obviously both these parameters, $C$ and $\psi$ would tend to unity for spherical particles. Finally, the "**Stokes diameter,** $d_{st}$," is defined as the diameter of the sphere of the same density and the same terminal settling velocity, $u_t$ as that of the particle.

$$d_{st} = \sqrt{\frac{18\,\mu\,u_t}{(\rho_p - \rho_o)g}} \qquad (4.6)$$

where $\rho_p$ and $\rho_o$ are the respective densities of the particle and the fluid, $\mu$ the dynamic viscosity of the fluid and $g$ the gravitational acceleration.

In the present chapter, unless indicated differently, the equivalent sphere diameter, $d_{pv}$ will be used for the characterization of non-spherical bulky particles, the subscript "$v$" will be dropped for simplicity.
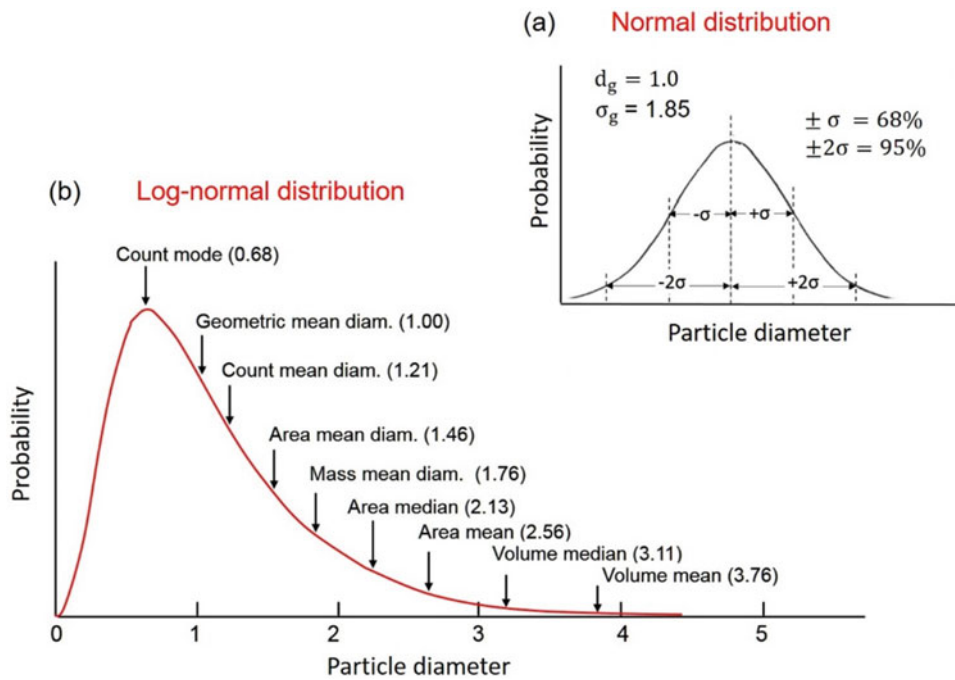
### 4.2.2   Particle Size-Distribution

When dealing with powders, it is most unlikely to have all of the particles of the same diameter. Powders are generally polydisperse when formed, some more than others depending on their manufacturing process. Proper representation of the particle size requires a statistical analysis of the particle size distribution (PSD) of a representative sample of the powder that could be carried out using optical or electron microscopy coupled with a detailed image analysis, light diffusion or instruments based on the particle terminal settling velocity, or mechanical screening using a set of calibrated sieves. The results could then be presented in graphical or in terms of key statistical parameters. Most random phenomena in nature can be represented by the standard normal distribution shown in right-hand side of Fig. 4.6 represented by the relationship:

$$F(x) = \frac{1}{\sigma_x\sqrt{2\pi}} \exp\left(-(x - \bar{x})^2/2\sigma_x^2\right) \qquad (4.7)$$

where $\bar{x}$ and $\sigma_x$ are, respectively, the mean value and standard deviation defined as:

$$\bar{x} = \frac{\displaystyle\sum_{i=1}^{\infty} n_i x_i}{\displaystyle\sum_{i=1}^{\infty} n_i} \qquad (4.8)$$

**Fig. 4.6** Normal and Log-normal particle size distribution, after Reist (1993)

and

$$\sigma_x = \left[ \frac{\sum_{i=1}^{\infty} n_i (x_i - \overline{x})^2}{\left( \sum_{i=1}^{\infty} n_i \right) - 1} \right]^{\frac{1}{2}} \quad (4.9)$$

Statistically, a variable with a normal distribution will have a 68% probability to be within $\pm \sigma_x$, and 95% probability to be within $\pm 2\sigma_x$.

For a variable to have a normal statistical distribution, it has to have equal probability to have a higher or lower value relative to its mean value (Fig. 4.6a). This condition is rarely satisfied for particle size distributions of powders that tend generally to be biased toward the finer size fractions. These distributions, however, would fit a normal distribution if the probability is plotted against the logarithm of the particle diameter giving rise to what is known as "lognormal distributions" as shown in lower LHS of Fig. 4.6b. The corresponding parameters for such a distribution are indicated on the curve.

These can be calculated as follows:

Geometric mean diameter, $\overline{d_g}$ and geometric standard deviation, $\sigma_g$ are defined for a number particle size distribution as:

$$log\,\overline{d_g} = \frac{\sum n_i log\,d_i}{\sum n_i} \quad (4.10)$$

and

$$log\,\sigma_g = \left[ \frac{\sum n_i \left( log\,d_i - log\,d_g \right)^2}{\sum n_i - 1} \right]^{\frac{1}{2}} \quad (4.11)$$

The corresponding values for a particle size distribution in terms of mass fraction rather than number fraction are given as:

$$log\,\overline{d_g} = \frac{\sum n_i d_i^3 log\,d_i}{\sum n_i d_i^3} \quad (4.12)$$

and

$$log\,\sigma_g = \left[ \frac{\sum n_i d_i^3 \left( log\,d_i - log\,d_g \right)^2}{\sum n_i d_i^3 - 1} \right]^{\frac{1}{2}} \quad (4.13)$$

It is important to note the fundamental difference between these two types of particle size distributions since in a number distribution the fine particles are given the same weight as any large particles in the powder and the distribution is accordingly biased toward fine particle presentation. The effect is clearly demonstrated in Fig. 4.7, which shows the same particle size histogram or frequency distribution function, represented both in terms of number fraction and mass fraction of the particles. For most engineering applications, the mass fraction distribution is the most pertinent since it reflects the mass distribution of the powder between different particle sizes.
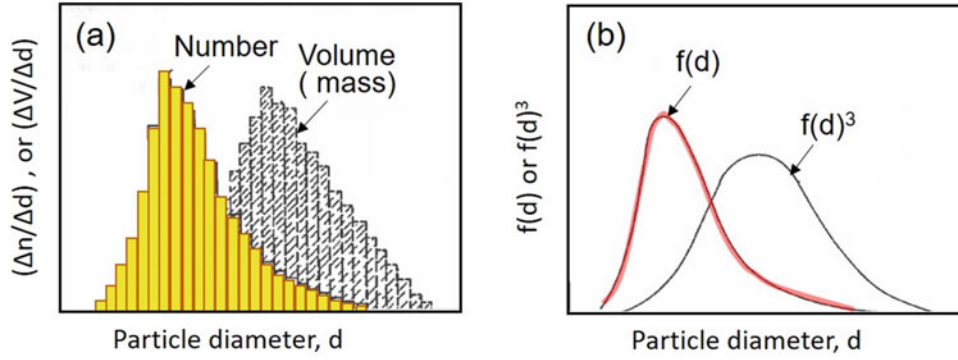
**Fig. 4.7** Particle size histogram and frequency distribution function presented in terms of number and mass fraction distributions, after Lefebvre (1989)

## 4.3    Plasma–Particle Momentum Transfer

While particles used in thermal spray tend to be of wide range of sizes and shapes, analysis of the plasma–particle interactions is developed for the simple geometry of a spherical particle in an infinite plasma stream. The justification for such an approach is based on the notion that most particles used tend to be of a considerably smaller dimension compared with the characteristic dimensions of the plasma and that once melted the particles acquire a spherical shape due to surface tension effects. Only during the initial part of the trajectory of a particle in a plasma its original shape is maintained. Non-spherical bulky particles could then be treated using an equivalent particle volume diameter, Eq. 4.3 combined with a corresponding shape factor if necessary such as the sphericity, given by Eq. 4.5.

### 4.3.1    Flow around Single Sphere and Drag Coefficient

The flow around a single sphere or any blunt body has been the subject of intensive study for many decades mostly with regard to aerospace, environmental, and chemical engineering applications. Numerous textbooks on the subject are available in literature, such as Clift et al. (1978) and Rudinger (1980). According to these studies, the flow field around a single sphere is governed by the standard Navier–Stokes (N–S) equations, which represents a balance between the inertia and viscous forces characterized by the Reynolds number, Re, in defined as:

$$Re = \frac{\rho\, u_R\, d_p}{\mu} \qquad (4.14)$$

where

$\rho$ mass density of the fluid (kg/m$^3$)
$\mu$ dynamic viscosity of the fluid (Pa.s)

$d_p$ diameter or characteristic dimension of the particle (m),
$u_R$ relative velocity between the fluid and the particle defined as

$$u_R = \sqrt{\left(u - u_p\right) + \left(v - v_p\right)} \qquad (4.15)$$

With, $u$ and $u_p$ are, respectively, the fluid and particle velocities in the axial direction (m/s), while $v$ and $v_p$ represent the corresponding fluid and particle velocities in the radial direction (m/s).

For a single sphere at very low Reynolds numbers (RE <0.01), the inertia forces are negligible compared with the viscous forces, the N–S equation can then be solved analytically giving rise to a symmetrical streamline upstream and downstream of the particle, as shown on the LHS of Fig. 4.8a. With the gradual increase of the Reynolds number in the range (0.01< RE <1.0) the flow remains dominated by viscous effects though with a loss of the upstream to downstream symmetry of the flow as illustrated by the Oseen solution given in the RHS of Fig. 4.8b.

With the further increase of the Reynolds number, the flow on the downstream side of the particle starts to show the beginning of flow separation at values of RE = 10 with full wake formation behind the sphere taking place at higher Reynolds number as shown in Fig. 4.9 after Taneda (1956). Beyond a Reynolds number of 130–200 vortex shedding downstream of the sphere starts reaching an intense level at a Reynolds number above 1000 as shown in Fig. 4.10.

Such important changes in the flow pattern around the particle have a direct impact on the drag coefficient, $C_D$ between the particle and its surrounding defined as the ratio of the drag force per unit projected surface area of the particle ($F_D/A_p$) and the fluid inertia forces ($\frac{1}{2}\, \rho U_r^2$).
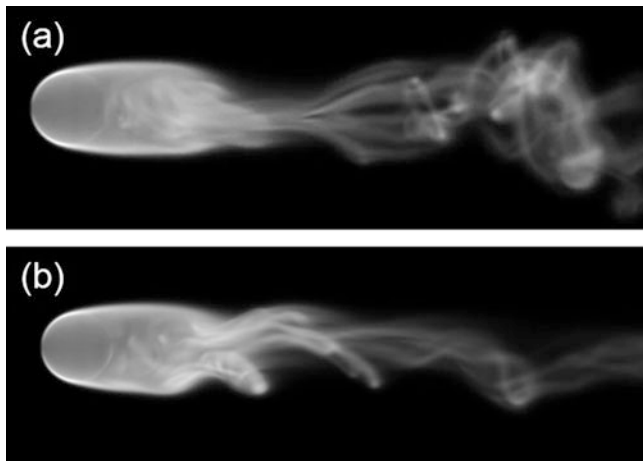
$$C_D = \frac{\left(F_D/a_p\right)}{\left(\frac{1}{2}\, \rho u_R^2\right)} \qquad (4.16)$$
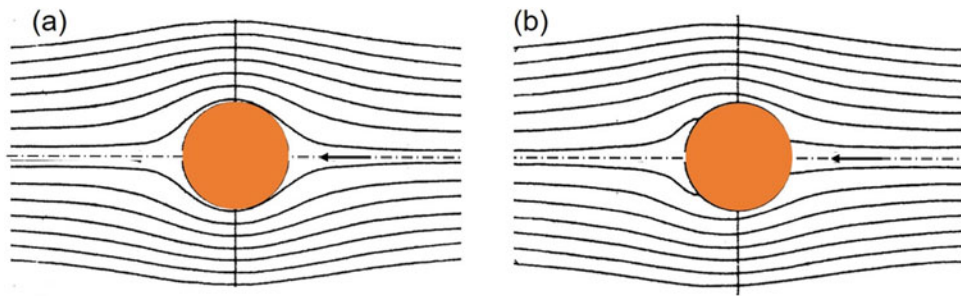
**Fig. 4.8** Streamlines over a spherical particle at low Reynold numbers (**a**) Re < 0.01 Stoke's flow (**b**) 0.01 < Re < 1.0 Oseen approximation, after Clift et al. (1978)
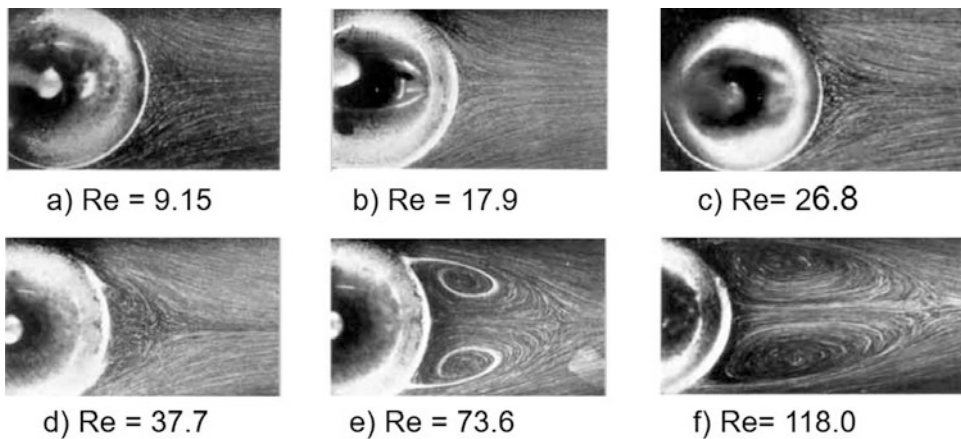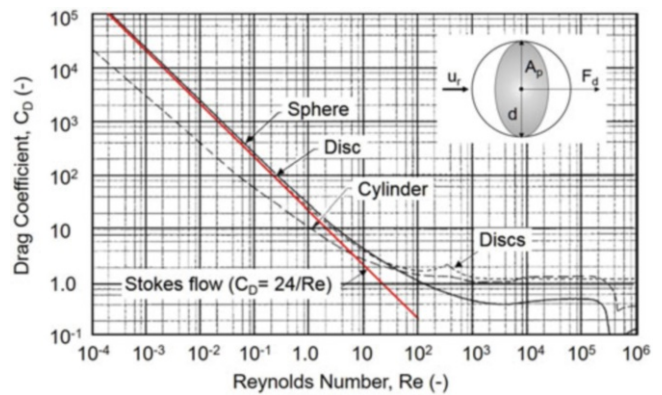


**Fig. 4.9** Flow visualization around a spherical solid particle at Reynolds numbers between 9 and 120. Flow from left to right, after Taneda (1956)



**Fig. 4.10** Flow visualization of vortex shedding in the wake of a sphere at ambient temperature



**Fig. 4.11** Drag coefficient as function of the Reynolds number for a single sphere, a cylindrical body, and a disc, after Lapple and Shepherd 1940

where

$F_D$ is total drag force exerted by the fluid on the particle (N),
$a_p$ is projected surface area of the particle perpendicular to the flow ($a_p = \pi d_p^2 /4$) (m$^2$).

The evolution of the drag coefficient, $C_D$ as function of the Reynolds number, $Re$, for a sphere, a circular disc and a cylindrical object are given in Fig. 4.11. These are mostly based on flow modeling studies and experimental data under normal ambient temperatures and pressures. For the case of a

**Table 4.1** Drag coefficient for a single sphere as function of the Reynolds number

| | |
|---|---|
| $C_D = \frac{24}{Re}$ | $Re \leq 0.2$ |
| $C_D = \frac{24}{Re}\left(1 + 0.1\ Re^{0.99}\right)$ | $0.2 < Re \leq 2$ |
| $C_D = \frac{24}{Re}\left(1 + 0.11\ Re^{0.81}\right)$ | $2 < Re \leq 20$ |
| $C_D = \frac{24}{Re}\left(1 + 0.189\ Re^{0.62}\right)$ | $20 < Re \leq 500$ |
| $C_D = 0.44$ | $Re > 500$ |

**Table 4.2** Correlations for the drag coefficient for a single sphere as function of the Reynolds number, after Oberkampf and Talpallikar (1994)

| | |
|---|---|
| $C_D = \frac{24}{Re}$ | $Re < 1$ |
| $C_D = \frac{24}{Re}(1 + 0.15\ Re^{0.687})$ | $1 < re < 1000$ |
| $C_D = 0.44$ | $Re > 1000$ |

sphere moving in a fluid at Reynolds number less than unity, known as the Stokes flow regime, the drag on the sphere is governed mainly by viscous forces, with the drag coefficient inversely proportional to the Reynolds number ($C_D = 24/Re$). At higher Reynolds number ($Re > 1$), the increase of the inertia forces gives rise to what is known as "form drag," which is responsible for the deviations of the drag coefficient from the Stokes flow relationship. Beyond $Re = 10^3$, up to $10^5$, the drag coefficient remains essentially constant at around 0.44, which is predominantly governed by form drag. During the plasma spraying of micrometer sized powders, the range of Reynolds number is rarely above 100 because of the relatively small particle diameter ($10 < d_p < 100$ μm) normally used. The drag confident over this range is best evaluated using the curve-fitted correlations given in Table 4.1. Alternate correlations proposed by Oberkampf and Talpallikar (1994) for Reynolds numbers in the range 1–1000 are given in Table 4.2. The correlation given by Eq. 3.17 was proposed by White (1974) for the Reynolds number range $Re < 100$.

$$C_D = \frac{24}{Re} + \frac{6}{1 + Re^{0.5}} + 0.4 \quad Re < 100 \qquad (4.17)$$

### 4.3.2   Corrections to the Drag Coefficient

Under thermal plasma conditions whether for plasma spraying, powder spheroidization, or chemical synthesis, the presence of steep temperature gradients across the boundary layer surrounding the particle has a significant effect on the flow field around the particle and consequently on momentum and heat exchange between the plasma and the particle. Special attention has, therefore, to be given to the

correction of the drag and heat transfer coefficients predicted using standard correlations obtained under normal temperatures and pressures. Other corrections may also be necessary under rarified flow conditions mostly encountered during low-pressure plasma spraying. Under these conditions, the mean free path of the gas molecules at high temperature can reach a few μm, which starts to be comparable with the characteristic dimension of the particles. Non-continuum effects, often referred to as Knudsen effect, can be important in this case and require special corrections to the drag coefficient predicted using continuum fluid mechanics.

#### 4.3.2.1  Effect of the Temperature Gradients

As discussed by Boulos et al. (1994), the plasma temperature outside the boundary layer surrounding a particle can exceed 10,000 K, while the particle surface temperature may not exceed 3000 K. Such a condition will give rise to steep temperature gradients across a boundary layer over a few hundreds of micrometers thick, causing strong non-linear variations of transport properties Lee et al. (1981). As a first approximation, Lewis and Gauvin (1973) proposed to evaluate the thermodynamic and transport properties used for the calculation of the drag and heat transfer coefficients based on the arithmetic mean film temperature, $T_f$, across the boundary layer surrounding the sphere:

$$T_f = \frac{(T_s + T_\infty)}{2} \qquad (4.18)$$

where $T_s$ is the surface temperature of the sphere and $T_\infty$ is the free stream plasma temperature. In a subsequent study, Sayegh and Gauvin (1979) carried out computations of the flow and temperature fields surrounding a spherical particle moving into an argon plasma at a Reynolds number of 50, assuming in one case constant fluid properties across the boundary layer, and in another case variable properties. The results presented in Fig. 4.12 were obtained for a sphere surface temperature, $T_s = 0.25 \times T_\infty$. These are presented in terms of stream lines, and temperature isocontours, $T^*$ is defined as ($T^* = T/T_\infty$) with the constant fluid property case presented on the lower part of the figure, while the variable property results are presented on the upper part of the figures, respectively.

Based on these results, Sayegh and Gauvin (1979) recommended the estimation of the fluid properties (kinematic viscosity, $\nu = \mu/\rho$, and thermal conductivity, $\kappa$, at a reference temperature defined as $T_{0.19}$, where

$$T_{0.19} = T_s + 0.19\,(T_\infty - T_s) \qquad (4.19)$$

Numerous other corrections for the effect of temperature gradients across the boundary layer on the drag and the heat
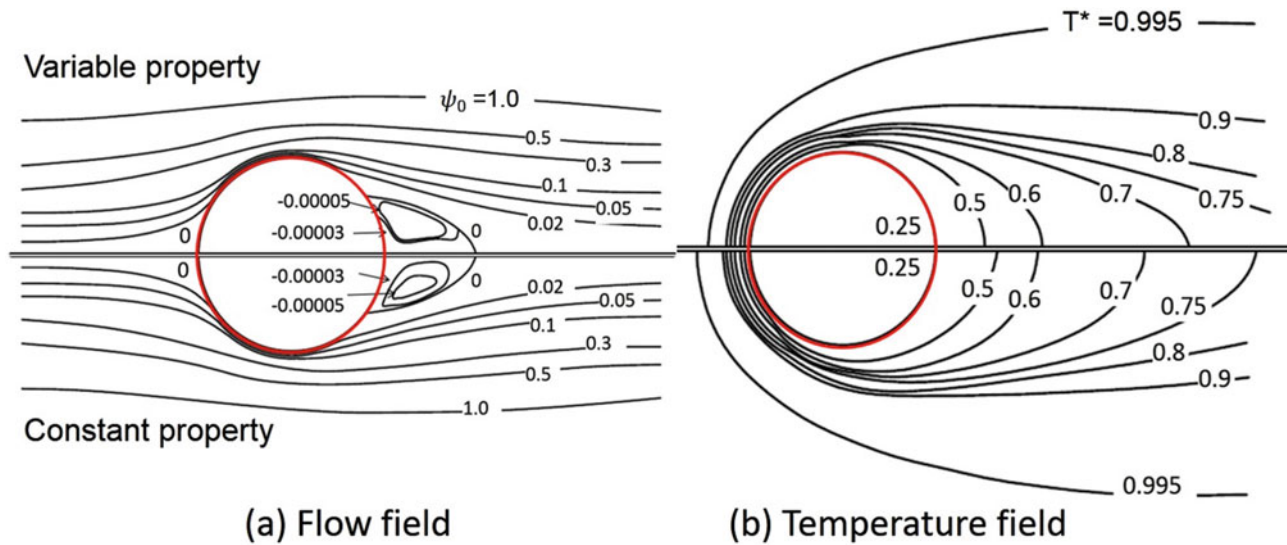
**Fig. 4.12** (**a**) Streamlines and (**b**) temperature isocontours for constant and variable fluid property flows, $N_{Re} = 50$, $T_s = 2500$ K, $T_\infty = 10,000$ K, $T^* = \frac{T}{T_\infty}$, after Sayegh and Gauvin (1979)

**Table 4.3** Drag coefficients for an argon plasma calculated using different correction factors Pfender and Lee (1985) and Pfender (1989)

| $T_s$(K) | $T_\infty$(K) | Reference | Reynolds number | | | | |
|---|---|---|---|---|---|---|---|
| | | | 0.1 | 1.0 | 10 | 20 | 50 |
| 1000 | 4000 | Simulation by Lee et al. (1982) | 100.8 | 15.4 | 2.9 | 1.8 | 1.0 |
| | | Properties evaluated at film temperature | 100.6 | 12.3 | 2.4 | 1.6 | 1.1 |
| | | Lee et al. (1981) | 115.6 | 14.2 | 2.7 | 1.9 | 1.2 |
| | | Lewis and Gauvin (1973) | 146.1 | 17.9 | 3.4 | 2.4 | 1.6 |
| 2500 | 10,000 | Simulation by Lee et al. (1982) | 151.9 | 17.6 | 3.3 | 2.1 | 1.2 |
| | | Properties evaluated at film temperature | 112.9 | 13.7 | 2.5 | 1.7 | 1.1 |
| | | Lee et al. (1981) | 136.9 | 16.6 | 3.1 | 2.1 | 1.4 |
| | | Lewis and Gauvin (1973) | 164.5 | 19.9 | 3.7 | 2.5 | 1.7 |
| 3000 | 12,000 | Simulation by Lee et al. (1982) | 199.9 | 22.4 | 4.2 | 2.6 | 1.4 |
| | | Properties evaluated at film temperature | 137.6 | 16.2 | 2.9 | 1.9 | 1.2 |
| | | Lee et al. (1981) | 202.3 | 23.9 | 4.2 | 2.8 | 1.8 |
| | | Lewis and Gauvin (1973) | 226.8 | 26.8 | 4.7 | 3.2 | 2.0 |

transfer coefficients have also been proposed and widely accepted in the literature (Pfender 1985). These involved the use of the mean film temperature defined by Eq. 4.18, for the estimation of the thermodynamic and transport properties of the plasma, followed by a further correction of the drag or heat transfer coefficient obtained. The ratio of kinematic viscosity estimated at the mean film temperature, $\nu_f$, to that estimated at the free stream temperature, $\nu_\infty$, to the power 0.15 was used giving rise to:

$$C_D = C_{Df} \left(\nu_f/\nu_\infty\right)^{0.15} \qquad (4.20)$$

where $C_{Df}$ is the drag coefficient evaluated at the mean film temperature $T_f$. Lee et al. (1981) proposed a different correction factor based on their computation's studies (performed mostly for argon):

$$C_D = C_{Df} \left(\rho_\infty\mu_\infty/\rho_s\mu_s\right)^{0.45} \qquad (4.21)$$

The index "s" means that the plasma properties are evaluated at the particle surface temperature $T_s$ and "∞," meaning properties are evaluated at the free-stream plasma temperature.

The difference between these two corrections, Eqs. 4.20 and 4.21, is well within the experimental error of the available data (± 25%). Results obtained with different expressions used for the correction of the drag coefficient in a DC plasma jet are summarized in Table 4.3. These show that, for a given Reynolds number, the drag coefficient calculated by different methods can vary by up to 50% between different correlations and simulation methods. They also show a strong dependence on the particle and free stream plasma temperatures.

### 4.3.2.2 Effect of Particle Shape

In all preceding discussion, the particles have been assumed to be spherical. While this is the case for agglomerated, spray-dried, atomized or spheroidized powders, it is not true for fused and crushed particles which, as shown earlier, can have angular shapes with a low shape factor. The shape of the particle modifies its drag coefficient (Ganser 1993), which, for example, can be correlated to the particle sphericity factor in a limited range of shape effects (Fukanuma et al. 2006). It must be emphasized, however, that particles when injected into the plasma are rapidly (~ a few tens of μs) heated to their melting temperature, thus attaining a spherical shape, which limits the effect of non-sphericity to the early part of their trajectory in the plasma close to their point of injection. The increase of drag force for spheroids compared with those for spheres with the same volume, may appreciably affect the particle trajectory, thus its temperature history in the plasma (Fukanuma et al. 2006; Xu et al. 2002). It is to be noted that the non-sphericity of the particles may also have a significant effect on the behavior of particles within the injector. More work is needed to understand and quantify this effect. Fukanuma et al. (2006) proposed that the influence of the shape of the particle on its drag coefficient can be correlated with the particle sphericity factor for a limited range of shapes. Equations have also been proposed to calculate the acceleration of non-spherical particles.

### 4.3.2.3 Non-continuum Effect

Other corrections that might be necessary when dealing with the transport and heating of fine particles ($d_p < 10$ μm) under plasma conditions, whether at atmospheric pressure or under soft vacuum conditions, are due to the non-continuum effect. These can be particularly important when the mean free path of the plasma, $\lambda$, is of the same order of magnitude as the diameter of the particles, $d_p$. Chen and Pfender (1983a, b) proposed the following correction to the drag coefficient in order to take into account the Knudsen effect, in the Knudsen number range ($0.01 < Kn < 1.0$),

$$C_D = (C_D)_{cont.} \left[ \frac{1}{1 + \left(\frac{2-a}{a}\right)\left(\frac{\gamma}{1+\gamma}\right)\frac{4}{Pr_s}(Kn)} \right]^{0.45} \quad (4.22)$$

where

$(C_D)_{cont.}$ drag coefficient evaluated using standard continuum fluid mechanics,

$Kn$ Knudsen number ($Kn = \lambda / d_p$)
$a$ thermal accommodation coefficient (−)
$d_p$ particle diameter (m)
$\lambda$ mean free path (m)

**Table 4.4** Knudsen numbers ($Kn$) for a 1 μm particles in plasmas at different absolute pressures and temperatures

| Pressure (kPa) | Temperature (K) | | | | |
| --- | --- | --- | --- | --- | --- |
| | 1000 | 3000 | 5000 | 7500 | 10,000 |
| 5 | 5.26 | 15.79 | 26.32 | 39.48 | 52.64 |
| 20 | 1.32 | 3.95 | 6.59 | 9.87 | 13.16 |
| 40 | 0.66 | 1.97 | 3.30 | 4.94 | 6.58 |
| 70 | 0.38 | 1.13 | 1.88 | 2.82 | 3.76 |
| 100 | 0.26 | 0.79 | 1.32 | 1.97 | 2.63 |

**Table 4.5** Correction factor to the Drag coefficient due to Knudsen effects for small zirconia particles immersed in an infinite Ar-H$_2$ (25 vol. % H$_2$) plasma at 10,000 K Fazilleau (2003)

| $d_p$ (μm) | 5.0 | 1.0 | 0.1 |
| --- | --- | --- | --- |
| $T_p = 1000$ (K) | 0.33 | 0.17 | 0.06 |
| 2000 | 0.28 | 0.14 | 0.05 |
| 3000 | 0.26 | 0.13 | 0.046 |

$\gamma$ specific heat ratio ($\gamma = c_p/c_v$)
$Pr_s$ Prandtl number of the gas at the surface temperature of the particle

Typical values of the Knudsen number for a 1 μm particle in an argon plasma at different absolute pressures and temperatures are given in Table 4.4. Numerical values of the correction factor, in square brackets, vary from 1.0 to 0.4, with the increase of the Knudsen number from 0.01 to 1.0. The correction to the drag coefficient can be important when considering particles in the size range 0.1 to 5 μm as used in suspension plasma spraying. This is illustrated in Table 4.5 from Fazilleau (2003), related to zirconia particles immersed in an infinite Ar-H$_2$ (25 vol. % H$_2$) plasma at 10,000 K.

### 4.3.2.4 Effect of Particle Charging

Particle charging can also have a limited effect on its trajectory in plasma jets, since a particle injected into thermal plasma will always assume a negative charge due to the difference between the thermal velocities and mobilities of electrons and ions. Whether or not this affects particles drag in thermal plasmas has never been explored. Chen and Ping (1986), Pfender (1989) and Chyou and Pfender (1989) have shown that under LTE conditions, particle charging will be of minor importance, because of the low charge concentration that can exist in the region near the particle surface. This may, however, be different for frozen chemistry, under non-continuum conditions in the case of low-pressure plasma spraying.

Deviations from LTE conditions in the plasma can also be important, particularly close to the particle surface. Whether or not such deviations will substantially affect heat and

momentum transfer to particles in the condensed phase, remains a matter for further study. Studies of momentum and heat transfer between low-pressure plasma and particles are generally based on molecular dynamics and they are beyond the scope of this book. The interested reader can find information in references Chen and Chen (1989), Uglov and Gnedovets (1991), Soo (1967).

## 4.4 Plasma–Particle Heat Transfer

As illustrated in Fig. 4.13, a single spherical particle immersed in a plasma will exchange heat with its surrounding by conduction, convection, and radiation. The net energy received by the particle, $Q_n$, is given by Eq. 4.23, which represents a simple energy balance between heat received by the particle from the plasma by conduction and convection, $Q_{cv}$, and heat lost by radiation from the surface of the particle to the surrounding, $Q_{sr}$.

$$Q_n = Q_{cv} - Q_{sr}$$
$$= h \, a_p \, (T_\infty - T_s) - A_p \, \varepsilon \, \sigma_s \, (T_s^4 - T_a^4) \quad (4.23)$$

where

$h$ heat transfer coefficient (W/m². K)
$a_p$ surface area of the particle, for a sphere $a_p = \pi \, d_p^2$ (m²)
$T_\infty$ the free-stream plasma temperature (K)
$T_s$ the surface temperature of the particle (K)
$\varepsilon$ particle emissivity (varies from 0 to 1.0)
$\sigma_s$ Stephan–Boltzmann constant ($5.67 \times 10^{-8}$ W/m². K⁴)

It is to be noted that any heat received by the particle as a result of radiation from the hot plasma is neglected since the plasma is generally considered as optically thin and the radiation incident angle is small.

The key parameter that needs to be specified in Eq. 4.23 is the heat transfer coefficient h, which is function of the relative velocity between the plasma and the particle, the composition of the plasma and its thermodynamic and transport properties.

$$Q_{CV} = h \, a_p \, (T_\infty - T_s) \qquad Q_{sr} = a_p \, \varepsilon \, \sigma_s \, (T_s^4 - T_a^4)$$
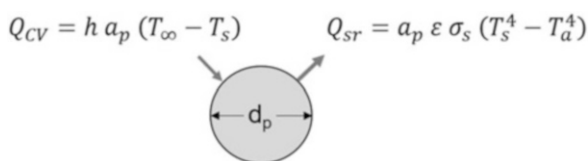


**Fig. 4.13** Schematic representation of the net heat exchanged between a particle and its surrounding

## 4.4.1 Heat Transfer Coefficient

The heat transfer coefficient, h, between the plasma and the particle may be expressed in terms of the Nusselt number, $Nu$, defined as:

$$Nu = \left(\frac{h d_p}{\kappa}\right) \quad (4.24)$$

where $d_p$ is the particle diameter and $\kappa$ is the thermal conductivity of the plasma in the boundary layer surrounding the particle. For a spherical particle immersed in an infinite plasma of uniform temperature, in the absence of any convention effects, it can be demonstrated that $Nu = 2.0$. In the presence of a relative motion between the particle and the plasma, a boundary layer develops around the sphere as shown earlier in Figs. 4.8, 4.9 and 4.10 giving rise to the gradual increase of the Nusselt number as a function of the Reynolds number, Re, and the Prandtl number, Pr. The data given in Fig. 4.14. are for heat transfer between a single sphere and air under normal temperature and pressure conditions. At low Reynolds numbers, the data can be correlated by the Ranz–Marshall correlation, Eq. 4.25 which is valid for $Re < 200$ and $0.5 < Pr < 1.0$,

$$Nu = 2.0 + 0.6 \, Re^{0.5} Pr^{0.33} \quad (4.25)$$

For gases other than air and in the presence of steep temperature gradients in the boundary layer surrounding the particle, a number of corrections have been proposed to the Ranz–Marshall equation as discussed in the next sections.

## 4.4.2 Corrections to the Heat Transfer Coefficient

### 4.4.2.1 Effect of the Temperature Gradients

As with the case of corrections to the drag coefficient under plasma conditions, corresponding efforts were devoted to the identification of the best approach to account for the significant variation of the thermodynamic and transport properties in the boundary layer surrounding the particle in a plasma flow and its influence on the heat transfer coefficient. As a first approximation, Lewis and Gauvin (1973) suggested the use of the mean film temperature, $T_f$, defined as, $T_f = (T_s + T_\infty)/2$, for the evaluation of the fluid properties used in the calculation of the Reynolds, Prandtl, and Nusselt numbers. A correction factor in the form of the kinematic viscosity ratio to the power 0.15 was also included in a modified form of the Ranz–Marshall equation for pure argon as follows:
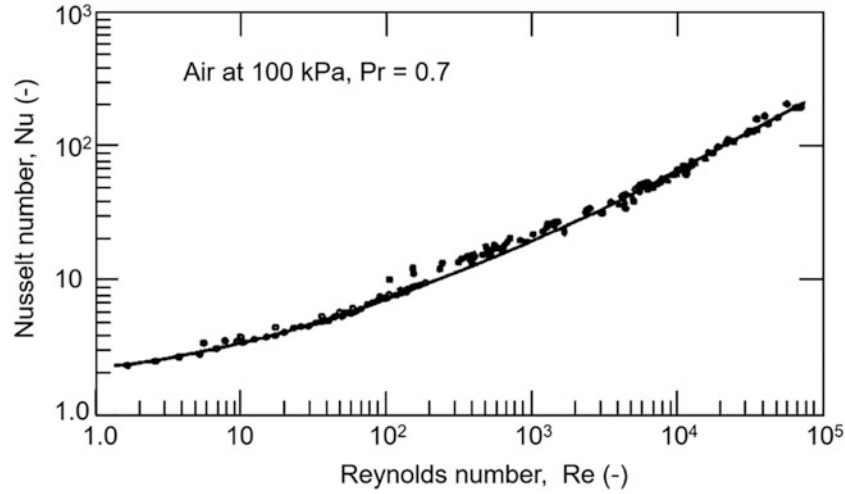
**Fig. 4.14** Nusselt number as function of the Reynolds number for a single sphere in air, Pr = 0.7, after Clift et al. (1978)

$$Nu = \left(2.0 + 0.515 \ Re^{0.5}\right)\left(v_f/v_\infty\right)^{0.15} \qquad (4.26)$$

Based on their modeling work for an argon plasma, Fig. 4.12, Sayegh and Gauvin (1979) proposed a similar approach as that used for the correction of the drag coefficient correction. This involved the calculation of the fluid properties at the reference temperature $T_{0.19}$ defined as $T_{0.19} = T_s + 0.19 \ (T_\infty - T_s)$ and to use the following rather complex empirical correlation for the calculation of the Nusselt number:

$$Nu = 2.0 \ f_0 + 0.473 \ Re^{0.552} Pr^m \qquad (4.27)$$

where

$$m = 0.78 \ Re^{0.552} \ Pr^{0.36} \qquad (4.28)$$

and

$$f_0 = \frac{\left(1 - T_0^{1+x}\right)}{\left[(1+x)(1 - T_0)T_0^x\right]} \qquad (4.29)$$

where $x$, the value of the exponent of $T$ in Eq. 4.29 relating the viscosity and the thermal conductivity to the absolute temperature ($x = 0.8$ for Ar at $T < 10{,}000$ K and $p = 100$ kPa).

Fizdon (1979), on the other hand, suggested using the following simpler correction:

$$Nu = \left(2.0 + 0.6 \ Re^{1/2} \ Pr^{1/3}\right)\left(\frac{\rho_\infty\mu_\infty}{\rho_s\mu_s}\right)^{0.16} \qquad (4.30)$$

where $Re$ and $Pr$ are calculated at the film temperature, $T_f$.

Lee et al. (1981) proposed the following slightly modified correlation:

$$Nu = \left(2.0 + 0.6 \ Re^{1/2} \ Pr^{1/3}\right)\left(\frac{\rho_\infty\mu_\infty}{\rho_s\mu_s}\right)^{0.6}\left(\frac{c_{p\infty}}{c_{p \ s}}\right) \qquad (4.31)$$

Chen and Pfender (1982a, b), Chen and Pfender (1983a, b) and Chen (1988) gave in a subsequent study an even more complex relationship:

$$Nu = 2.0\left[1.0 + 0.63 \ Re_\infty \ Pr_\infty^{0.8}\left(\frac{Pr_s}{Pr_\infty}\right)^{0.42}\left(\frac{\rho_\infty\mu_\infty}{\rho_s\mu_s}\right)^{0.52}C^2\right] \qquad (4.32)$$

in which,

$$C = \frac{1 - (h_s/h_\infty)^{1.1}}{1 - (h_s/h_\infty)^2} \qquad (4.33)$$

where $h_s$ and $h_\infty$, in Eq. 4.33, are the specific enthalpy of the plasma calculated, respectively, at the particle surface temperature $T_s$, and the free-stream plasma temperature $T_\infty$.

The values of the Nusselt number obtained using these different correlations and computation schemes are given in Fig. 4.15 for an atmospheric argon plasma at 4000 K, as function of the Reynolds number (Pfender 1985). While these are reasonably consistent at moderate plasma temperatures, significant difference is observed at plasma temperatures above 10,000 K due to ionization and recombination effects.

These differences are particularly important when considering diatomic gases such as Ar-H$_2$ (17 vol % H$_2$) mixture. This is
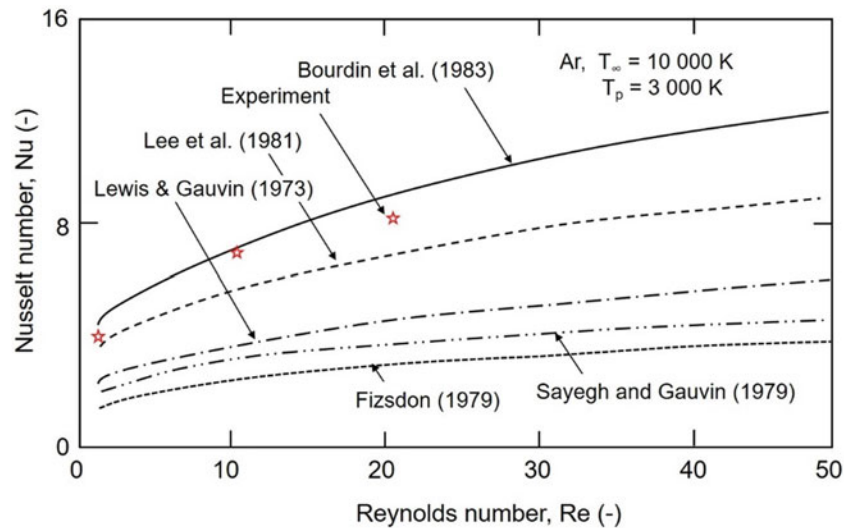
**Fig. 4.15** Nusselt number derived by different authors and by computer simulation, after Pfender (1985)
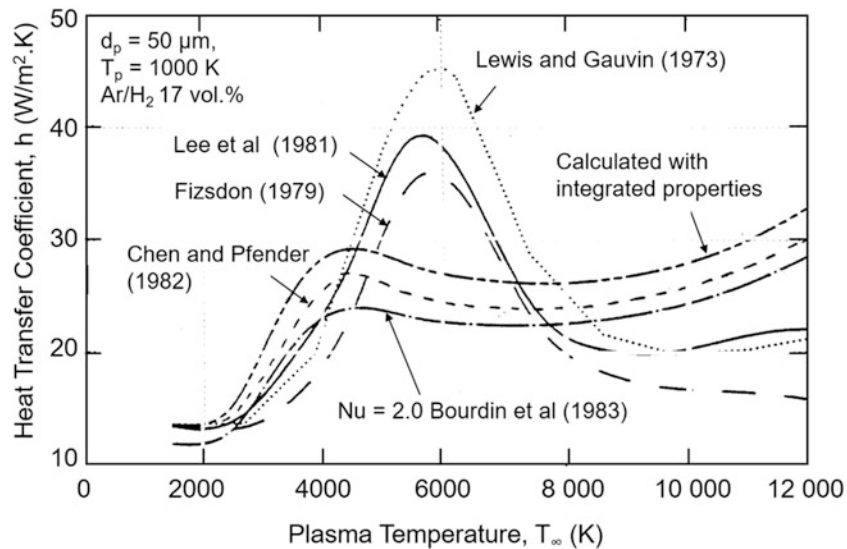


**Fig. 4.16** Heat transfer coefficient for a 50 μm diameter particle travelling at 50 m/s with $T_s = 1000$ K in an Ar-H$_2$ (17vol.%) plasma calculated by Vardelle (1988)

illustrated in Fig. 4.16, representing the heat transfer coefficients calculated by Vardelle (1988) versus temperature for a 50 μm particle, with a surface temperature, $T_s = 1000$ K, and relative velocity between the plasma and the particle of 50 m/s.

The results by Lewis and Gauvin (1988), Fizdon (1979), and Lee et al. (1981) in Fig. 4.16 were evaluated at $T_f$ and they exhibit similar evolution with a peak close to 6000 K corresponding to $T_f = (6000 + 1000)/2 = 3500$ K, that is, the dissociation temperature of hydrogen where $\kappa$, as well as $c_p$, exhibit high values. It can be seen that the difference between the values of the heat transfer coefficient, h, for pure conduction ($Nu = 2.0$, Bourdin et al. (1983) in Fig. 4.16) and that including convection effects (calculated with integrated properties in Fig. 4.16) is less than 20%.

Because of high temperature gradients and strong non-linear variations of the thermal conductivity, $\kappa$, with temperature, essentially for plasmas, one of the key problems for heat transfer coefficient calculations using the Nusselt number (Eq. 4.25) is to determine at which temperature the thermal conductivity has to be evaluated. It can be the film temperature $T_f$ (Eq. 4.26), $T_{0.19}$ (Eq. 4.27) or any other temperature. This problem is important when considering diatomic gases for which a strong peak of $\kappa$ is observed at the dissociation temperature of the gas.

A detailed theoretical analysis of the problem of pure conduction by Bourdin et al. (1983) showed that the standard heat transfer equation, Eq. 4.25 holds even under plasma
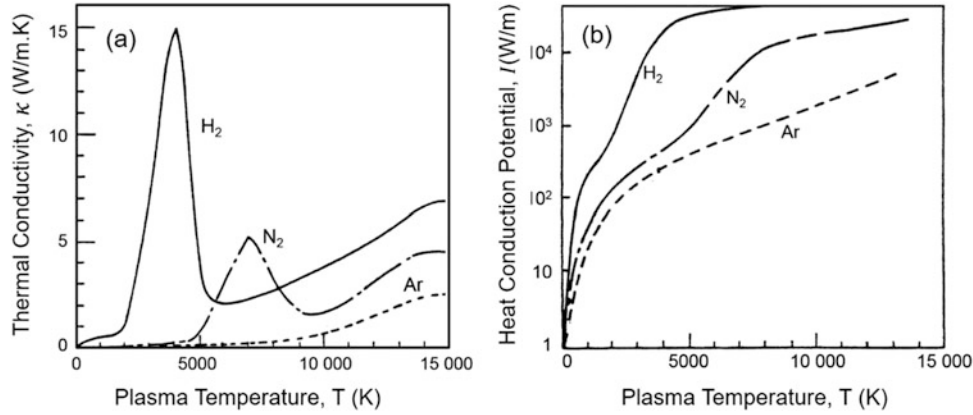
**Fig. 4.17** Thermal conductivity (**a**) and heat conduction potential (**b**) for different gases at atmospheric pressure as function of temperature, after Bourdin et al. reprinted with kind permission from Elsevier for Journal of Heat and Mass Transfer Bourdin et al. (1983)

conditions, provided that the properties are evaluated as an integrated mean value defined as:

$$\overline{\kappa} = \frac{1}{(T_\infty - T_p)} \left[ \int_{T_p}^{T_\infty} \kappa(T)dT \right] \quad (4.34)$$

It is interesting to note that if the thermal conductivity, $\kappa$ is a linear function of temperature, Eq. (4.34) reduces to the commonly used practice of evaluating the property values at the arithmetic mean, that is, $\overline{\kappa}(T) = \kappa(T_f)$, or film temperature.

The application of Eq. (4.34) can be considerably simplified by splitting the integral with respect to some reference temperature, $T_o = 300$ K, as follows:

$$\overline{\kappa} = \frac{1}{(T_\infty - T_p)} \left[ \int_{300}^{T_\infty} \kappa(T)dT - \int_{300}^{T_p} \kappa(T)dT \right] \quad (4.35)$$

$$\overline{\kappa} = \frac{1}{(T_\infty - T_p)} \left[ S(T_\infty) - S(T_p) \right] \quad (4.36)$$

where $S(T)$ is the heat conduction potential. Values of $\kappa$ and $S(T)$ are given in Fig. 4.17 for different plasma gases at atmospheric pressure as a function of temperature.

It should be noted that the analysis of Bourdin et al. (1983) is limited to pure conduction, which provides a reasonable estimate of the heat transfer to the particles considering that in most practical cases for plasma spraying ($Re < 20$ and $Pr < 1$) the convection term contributes less than 25% to the total heat transfer to the particles. Examples of the mean integrated thermal conductivity of Ar/H$_2$ and Ar/He plasmas at atmospheric pressure as function of temperature are given in Figs. 4.18 and 4.19, respectively. A comparison of the data for Ar/H$_2$–30 vol.% and Ar/He-60 vol.% is given in
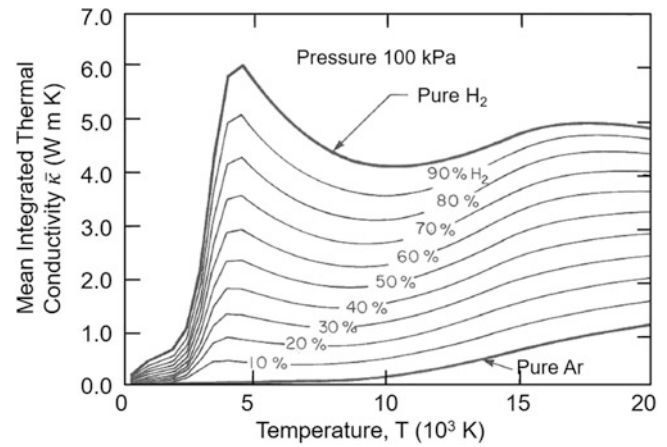


**Fig. 4.18** Mean integrated thermal conductivity of Ar/H$_2$ plasmas at atmospheric pressure as function of temperature
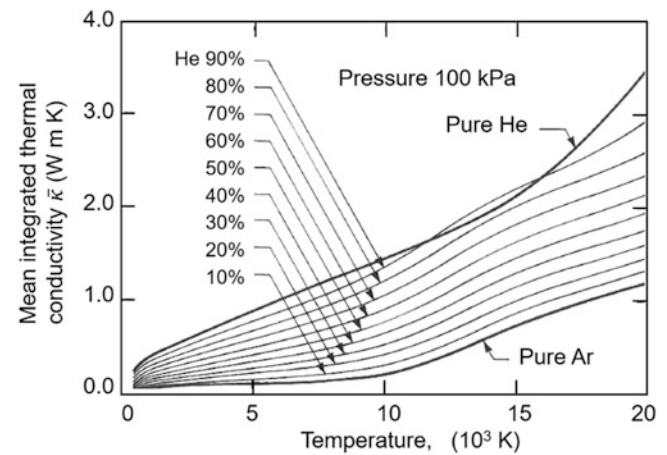


**Fig. 4.19** Mean integrated thermal conductivity of Ar/He plasmas at atmospheric pressure as function of temperature
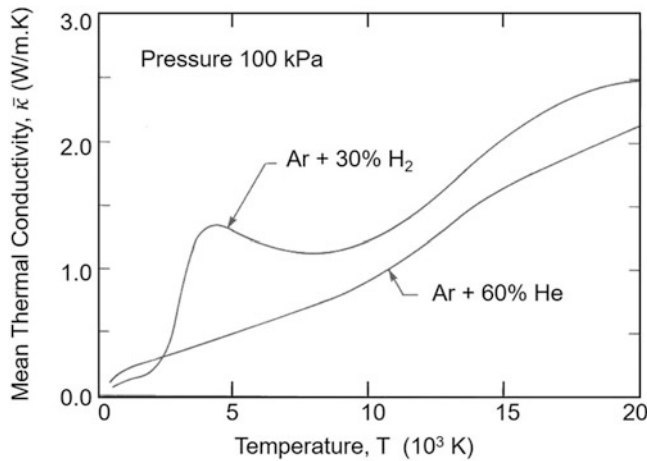
**Fig. 4.20** Mean integrated thermal conductivity of Ar/H$_2$ and A/He plasmas at atmospheric pressure as function of temperature



**Fig. 4.21** Limiting temperature for metallic particles immersed in atmospheric pressure Ar plasma, particle emissivity assumed to be unity, after Boulos (2004)

Fig. 4.20, showing a high mean thermal conductivity for the Ar/H$_2$ mixture (30 vol.%) compared with Ar/He (60 vol.%), in the 3000–6000 K temperatures range.
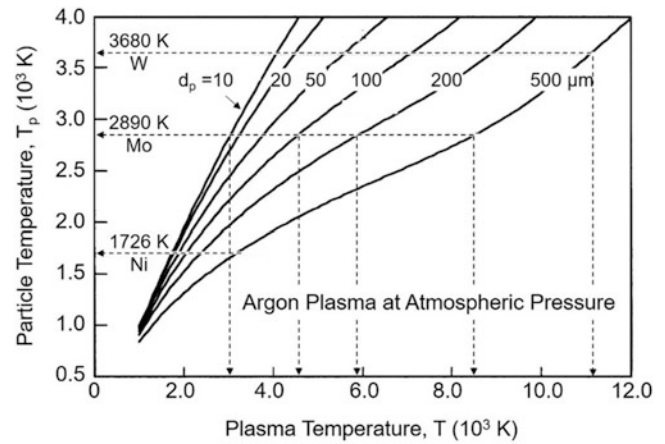
#### 4.4.2.2 Non-continuum Effect

The effect is quite similar to that observed for the drag coefficient using Eq. 4.22 with a thermal accommodation coefficient of 0.8. A corresponding correction to account for non-continuum effects in plasma–particle heat transfer over the same Knudsen number range *(0.01 < Kn < 1.0)* has also been proposed by Chen and Pfender (1983b). In this case, they made use of the concept of temperature jump, resulting in the following correction:

$$q = q_{cont.} \left[ \frac{1}{1 + (2 Z^*/d_p)} \right] \qquad (4.37)$$

where (q)$_{cont}$ is the heat flux calculated using an available correlation for continuum flow and Z$^*$ is the jump distance. Typical numerical values of the correction factor in square brackets in this case could be as low as 0.4 to 0.5 for a Knudsen number of about 0.1. It is important to note that the Knudsen effect is stronger for plasmas with higher enthalpies Chen and Pfender (1983b). For small particles (e.g., 0.1–5 μm), corrections with a magnitude similar to those already presented for C$_D$ have to be made (Fazilleau 2003).

### 4.4.3 Radiation Energy Losses from the Surface of the Particle

As stated earlier, Eq. 4.23, the net energy that contributes to the transient heating of the particle, is the difference between the heat received by the conduction and convention from the plasma, Q$_{cv}$, and heat lost by radiation from the surface of the particle to its surrounding, Q$_{sr}$.

$$
\begin{aligned}
Q_n &= Q_{cv} - Q_{sr} \\
&= h\, a_p\, (T_\infty - T_s) - a_p\, \varepsilon\, \sigma_s\, (T_s^4 - T_a^4) \qquad (4.23')
\end{aligned}
$$

Because of the dependence of the radiative energy losses on $(T_s^4 - T_a^4)$, Q$_n$ decreases rapidly with the increase of the particle surface temperature T$_s$ and eventually can be equal to zero or even acquire a negative value *even when the particle temperature is lower than that of the surrounding plasma*. At this point the particle temperature will remain constant (for $Q_n = 0$) or start cooling down ($Q_n < 0$). A conservative estimate of the limiting temperate that a particle can reach is obtained by equating the conduction heat transfer between the plasma and the particle ($Nu = 2.0$) with radiation losses as function of the surface temperature of the particle. Assuming the particle emissivity to be equal to unity allows for the calculation of limiting particle temperature that could be achieved as function of the plasma composition and temperature for particles of different diameters. Typical results obtained for an atmospheric pressure argon plasma are given in Fig. 4.21 Boulos (2004). These show for each particle diameter the gradual increase of the limiting particle temperature as function of the plasma temperature. The relationship is almost linear for particles of diameters less than 10 μm. With the increase of the particle diameter, radiation losses increase, requiring a higher plasma temperature to compensate for the increase of radiation losses. In specific terms if we consider, for example, a molybdenum particle with a diameter of 10 μm, immersed into an argon plasma, there would be no difficulty to melt the particle with a plasma temperature of about the same temperature as the melting
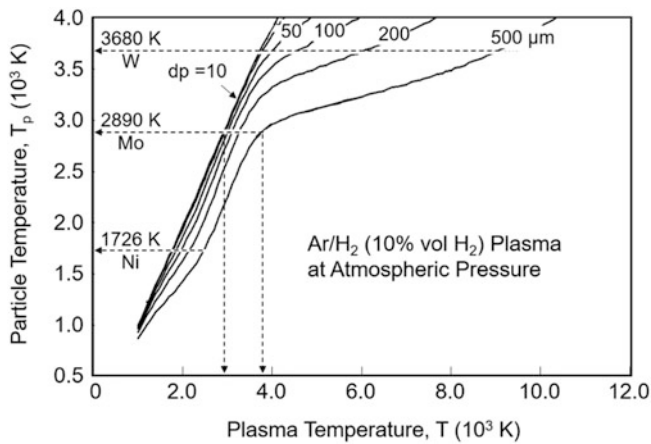
**Fig. 4.22** Limiting temperature for metallic particles immersed in atmospheric pressure Ar/H$_2$ 10 vol.% plasma, particle emissivity assumed to be unity, after Boulos (2004)
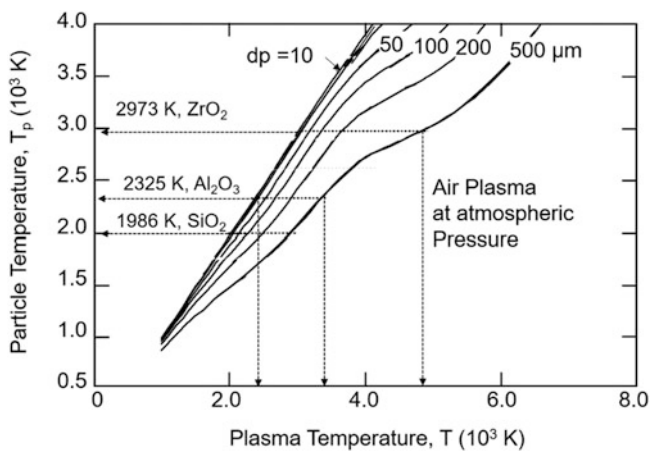


**Fig. 4.23** Limiting temperature for ceramic particles immersed in atmospheric pressure Air plasma, particle emissivity assumed to be unity, after Boulos (2004)

temperature of molybdenum (2890 K). In contrast, for a molybdenum particle with a diameter of 100 μm, the plasma temperature necessary for its melting would be 4500 K. Corresponding values for particles of diameters of 200 μm and 500 μm would be 6000 K and 8300 K, respectively. It is to be noted that these are asymptotic limiting temperatures in which the time of contact between the particles with the plasma is not limiting.

The limiting role of radiation losses from the surface of the particle becomes increasingly more important with the increase of the melting temperature of the material. A 500 μm tungsten particle (melting temperature 3680 K) would accordingly require an argon plasma temperature of more than 11,000 K to reach its melting temperature (Fig. 4.22). Corresponding data for an Ar/H$_2$ 10 vol.% H$_2$ plasma given in Fig. 4.22 reveal essentially the same trends,

though the effect is significantly reduced for materials of low to medium melting temperature such as Ni and Mo due to the high thermal conductivity of the Ar/H$_2$ plasma requiring a smaller temperature difference for compensating for radiation heat losses from the surface of the particle.

Similar effects are also observed in Fig. 4.23 for ceramic particles in an air plasma with the extended range of the required plasma temperature for melting of the ceramic increasing significantly for high temperature ceramic materials such as zirconia (ZrO$_2$) compared with Alumina (Al$_2$O$_3$) or Silica (SiO$_2$).

## 4.5    Transient Heating and Melting of a Particle

This section deals exclusively with the transient heat conduction inside a single spherical particle immersed in a thermal plasma. The analysis is largely based on the work of Chen and Pfender (1982a, b) and Bourdin et al. (1983), who were the first to address this relatively complex problem. For simplicity, the analysis is limited to conduction heat transfer between the plasma and the particle surface, which correspond to the case of a stationary particle inside an infinite plasma volume. The model formulation used is based on the following assumptions:

- Spherical particle immersed in an infinite plasma volume
- Negligible radiation losses and vaporization from the surface of the particle
- Conduction heat flux to the surface of the particle ($Nu = 2$)

The assumption that $Nu = 2$, implies the absence of convective heat transfer between the plasma and the particle and that the boundary layer relaxation time around the particle is short in comparison to the heating required for melting the particle.

Chen and Pfender (1982a, b) and Bourdin et al. (1983) independently further extended their analysis to the moving boundary problem during the melting phase of the particle. While the proposed model was solved for a dense spherical particle, it is equally applicable to porous particles through the use of an equivalent effective thermal conductivity of the particle material.

## 4.5.1    Spherical Particle with Infinite Thermal Conductivity

For a metallic particle with a high thermal conductivity, it is reasonable to assume the internal temperature gradients in the particle to be negligible and the particle is essentially at a uniform temperature. The evolution of the temperature of a

particle in this case, when suddenly immersed in a plasma environment, can be calculated by a simple energy balance on the particle as follows:

$$\frac{dT_p}{dt} = \frac{-12\,\overline{\kappa}}{\rho_p c_{ps} d_p^2}\,(T_p - T_\infty) \tag{4.38}$$

where

$T_p$ particle temperature
$T_\infty$ free-stream plasma temperature
$\overline{\kappa}$ integral mean thermal conductivity of the plasma
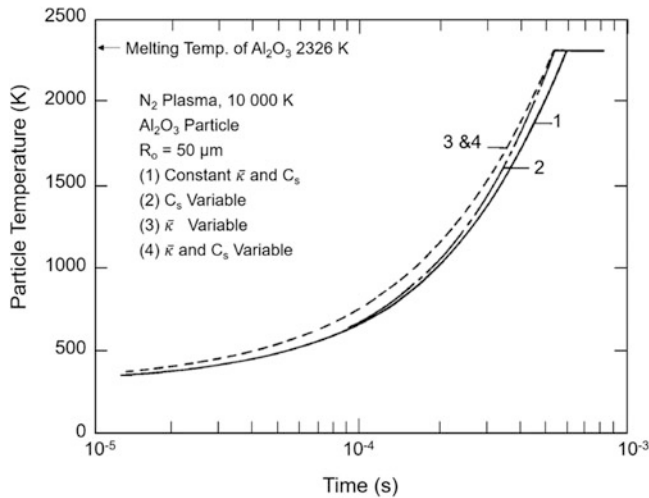$\rho_p$ density of the particle
$c_{ps}$ specific heat of the particle
$d_p$ particle diameter

Assuming constant thermodynamic properties of the material ($\rho_p$, $c_{ps}$) and transport properties of the plasma ($\overline{\kappa}$), it is possible to obtain an exact solution to Eq. 3.38, as follows:

$$\frac{T_p - T_\infty}{T_0 - T_\infty} = \exp\left(\frac{12\,\overline{\kappa}\,t}{\rho_p c_{ps} d_p^2}\right) \tag{4.39}$$

As expected, Eq. 4.39 gives rise to as faster increase of the particle temperature with the increase of the thermal conductivity of the plasma, and the decrease of the specific heat of the particle material. The effect of the different simplifying assumption on the predicted temperature history of a 100 μm alumina particle immersed in nitrogen plasma at 10,000 K can be identified in Fig. 4.24 where the transient temperature



**Fig. 4.24** Temperature history for a 100 μm alumina particle immersed in a nitrogen plasma at 10,000 K, assuming infinite thermal conductivity of the particle, Bourdin et al. (1983)

rise of the particle is plotted as function of time using assumptions Bourdin et al. (1983).

## 4.5.2   Effect of Internal Heat Conduction

The following assumptions are made:

- The particle is spherical with finite but constant specific heat and thermal conductivity.
- The particle has a uniform initial temperature, $T_0$ before being suddenly immersed in a plasma of a temperature $T_\infty$.
- Negligible radiation losses from the particle surface.
- The particle temperature is followed only to the point where its surface reaches the melting point of the material.

Bases on the above assumptions, the equation governing the transient heat transfer in the particle can be written as:

$$\frac{1}{\alpha_p}\frac{\partial T}{\partial t} = \frac{1}{r^2}\frac{\partial}{\partial r}\left(r^2\frac{\partial T}{\partial r}\right) \tag{4.40}$$

where

$\alpha_p$ thermal diffusivity of the particle material ($\alpha_p = \kappa_p/\rho_p c_{ps}$)

Equation 4.40 can be solved with the following boundary conditions:

$$t = 0, \quad 0 < r < R_0, \quad T(r,t) = 300\,K$$

$$t > 0 \quad\quad r = 0, \quad\quad \left.\frac{\partial T}{\partial r}\right|_{r=0} = 0$$

$$r = R_0 \quad \left.\kappa\frac{\partial T}{\partial r}\right|_{r=R_0} = q$$

where $q$ is the external heat flux to the surface of the particle given for $Nu = 2$, as follows:

$$q = \frac{2\overline{\kappa}}{d_0}\,(T_\infty - T_s) \tag{4.41}$$

The results obtained for the same conditions as those used in Fig. 4.24, that is, 100 μm diameter alumina particle suddenly immersed in a 10,000 K nitrogen plasma are given in Fig. 4.25. The computation is carried out in this case, included internal heat conduction into the particle. For comparison, the results obtained assuming a "uniform temperature of the particle" are superposed on the figure identified as the "simple case."

It is to be noted that when the surface temperature of the particle reaches its melting point 2326 K, the temperature of
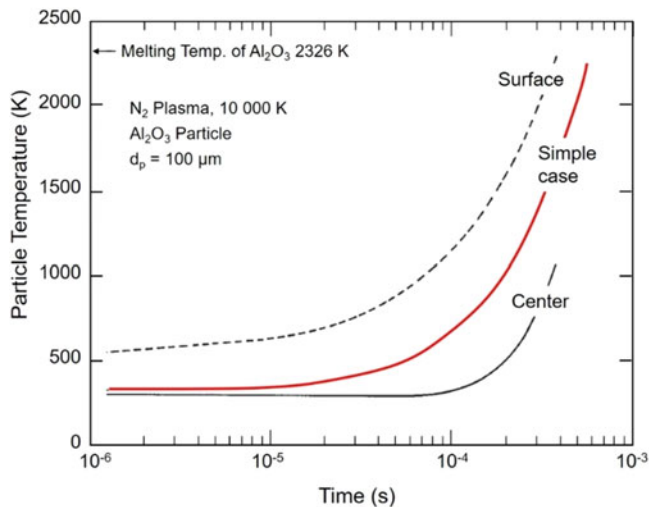
**Fig. 4.25** Temperature history for a 100 μm alumina particle immersed in a nitrogen plasma at 10,000 K, including internal heat conduction, Bourdin et al. (1983)
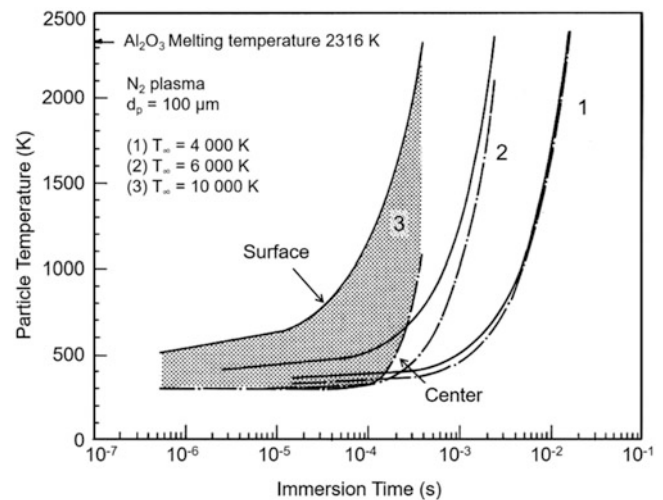


**Fig. 4.27** Temperature history of 100 μm diameter alumina particles immersed in nitrogen plasma at different temperatures, after Bourdin et al. (1983)
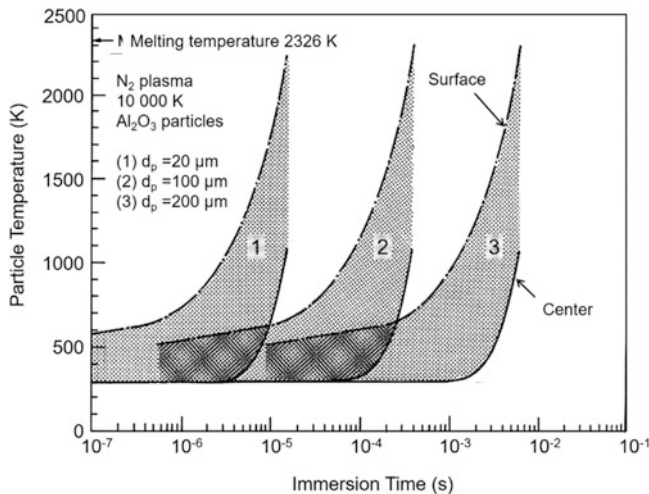


**Fig. 4.26** Temperature history of alumina particles of different diameters suddenly immersed in a nitrogen plasma at 10,000 K, after Bourdin et al. (1983)

the center of the particle will be lagging behind at 1075 K, which is 1251 K lower than that of the surface temperature. Obviously the so-called simple case, assuming an infinite thermal conductivity of the particle, while representing reasonably well the mean temperature of the particle, would be seriously an error in terms of internal temperature distribution in the particle.

Bourdin et al. (1983) carried out a systematic study of the transient heating of spherical particles of different materials (Ni, Si, $Al_2O_3$, W, $SiO_2$) and different particle sizes ($d_p$ = 20–400 μm) as they are suddenly immersed in different plasmas (Ar, $N_2$, $H_2$) at atmospheric pressure and temperatures varying between $T_\infty$ = 4000 and 10,000 K.

Typical results obtained for alumina particles of different diameters immersed in a nitrogen plasma at 10,000 K are given in Fig. 4.26. These show that the heating time of the particles depends strongly on the particle diameter with the surface temperature of the particles increasing at a much faster rate than its center. This gives rise to the development of significant internal temperature gradients in the particle with temperature differences between the surface of the particle and its center of the order of 1000 K independent of the particle diameter. As shown in Figs. 4.27 and 4.28, the effect is strongly dependent on the external heat flux to the particle, the lower the plasma temperature or the thermal conductivity of the plasma gas, the more uniform will be the temperature distribution in the particle. As noticed in Fig. 4.29, the effect is also dependent on the thermal conductivity of the particle material. The higher is the thermal conductivity of the particle the more uniform its internal temperature distribution.

Based on the above results Bourdin et al. (1983) concluded that a good estimate of the relative importance of the phenomena of internal heat conduction in the particle can be made based on the value of the *Biot number*, *Bi*, which represents the ratio of the mean integral thermal conductivity of the plasma across its boundary layer surrounding the particle, $\bar{\kappa}$ and the thermal conductivity of the particle material, $\kappa_p$ defined as:

$$Bi = \bar{\kappa}/\kappa_p \qquad (4.42)$$

As a general rule it was observed that important differences can exist between the surface temperature of the particle and that at its center, when the Biot number is larger than 0.03.
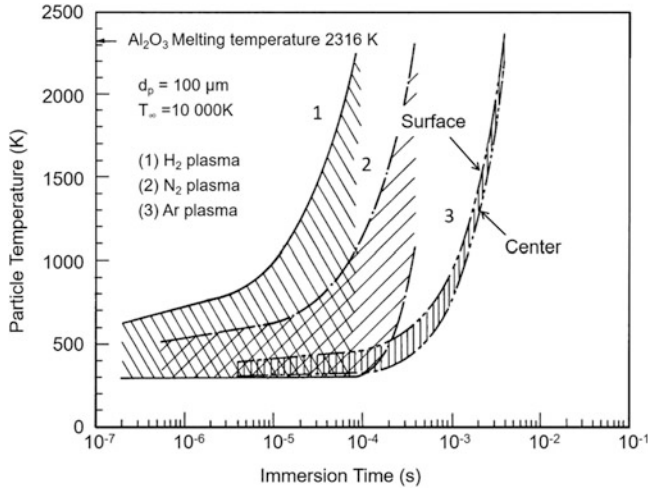
Fig. 4.28 Temperature history of 100 μm diameter alumina particles immersed in different plasmas at 10,000 K, after Bourdin et al. (1983)
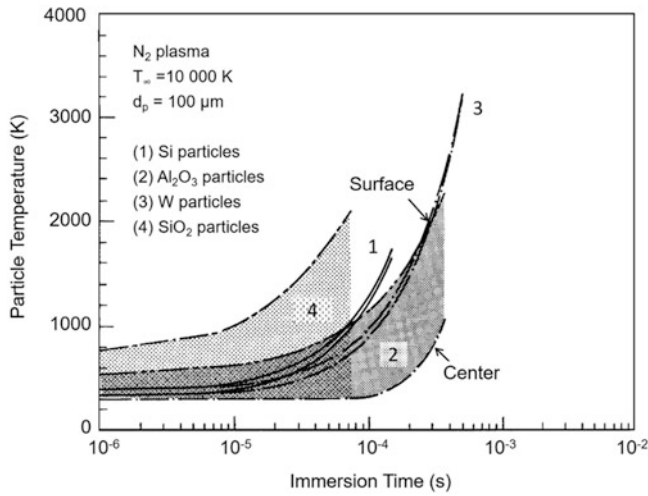


Fig. 4.29 Temperature history of 100 μm diameter particles of different materials immersed in a nitrogen plasma at 10,000 K, after Bourdin et al. (1983)

### 4.5.3 The Moving Boundary Problem

In the previous section dealing with internal heat conduction in the particles, results were given in which computations were limited to particle surface temperature below the melting point of the material. To take the computation beyond this point to include particle melting, the model formulation has to be modified including the propagation of the melting front as semantically represented in Fig. 4.30. The radius of the melting front, $r_m$ defines the boundary between the solid core of the particle $(0 < r < r_m)$ and molten region $(r_m < r < R_0)$. The governing equations, after Murray and Landis (1959), can be written for both regions of the particle as follows:
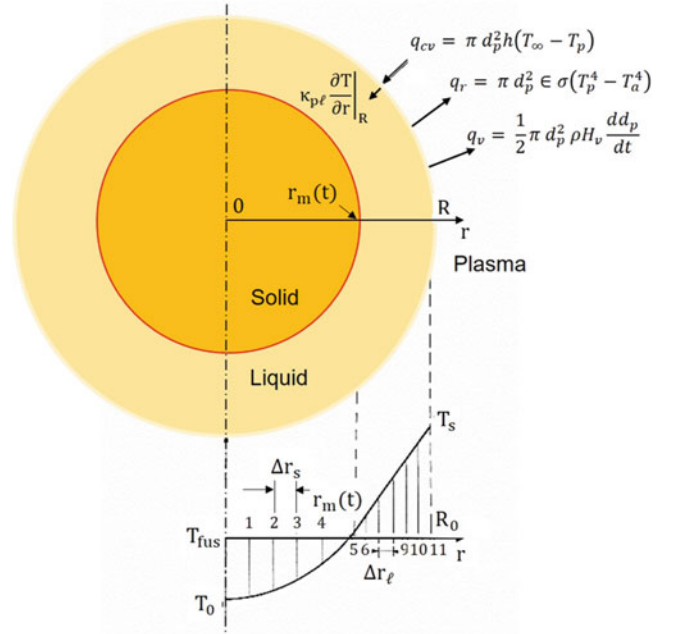


Fig. 4.30 Boundary conditions for the propagation of a melting front within a spherical particle Bourdin et al. (1983)

$$\frac{1}{\alpha_p} \frac{\partial T}{\partial r} = \frac{1}{r^2} \left[ \frac{\partial}{\partial r} \left( r^2 \frac{\partial T}{\partial r} \right) \right] \tag{4.43}$$

$$\frac{1}{\alpha_\ell} \frac{\partial T}{\partial r} = \frac{1}{r^2} \left[ \frac{\partial}{\partial r} \left( r^2 \frac{\partial T}{\partial r} \right) \right] \tag{4.44}$$

With $\alpha_p$, and $\alpha_\ell$ are, respectively, the thermal diffusivities of the particle material in the solid and liquids states, defined as $(\alpha_p = \kappa_p/\rho_p c_{ps})$ and $(\alpha_\ell = \kappa_\ell/\rho_\ell c_{p\ell})$.

The boundary conditions for Eqs. 4.43 and 4.44 are:

$$\text{at } r = 0 \quad \left. \frac{\partial T}{\partial r} \right|_{r=0} = 0 \tag{4.45}$$

and

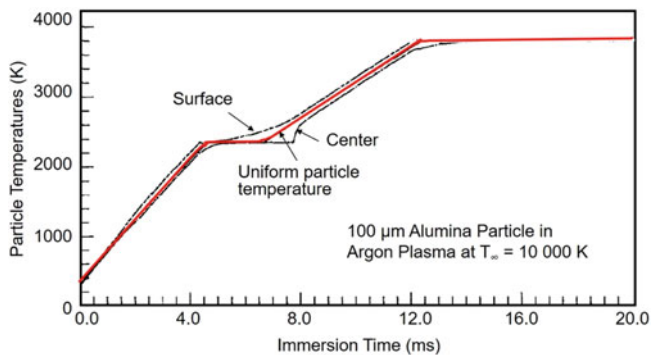$$\text{at } r = R_0 \quad \left. \frac{\partial T}{\partial r} \right|_{r=R_0} = q \tag{4.46}$$

at the solid–liquid interface, $r = r_m$, the velocity of propagation of the melting front is given by the equation:

$$\frac{\partial r_m}{\partial t} = \frac{1}{\rho H_m} \left[ \kappa_\ell \left. \frac{\partial T_\ell}{\partial r} \right|_{r=r_m} - \kappa_p \left. \frac{\partial T_s}{\partial r} \right|_{r=r_m} \right] \tag{4.47}$$
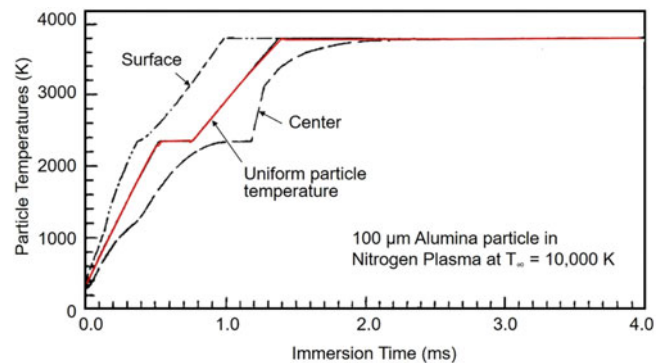
where
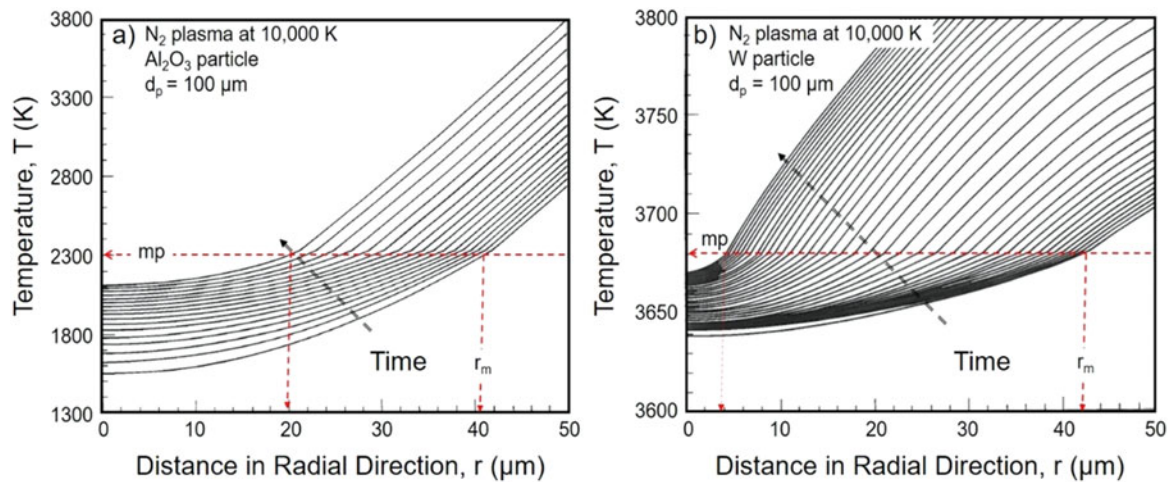
**Fig. 4.31** Transient heat propagation and melting of a solid spherical particle. (**a**) Alumina, (**b**) tungsten Bourdin et al. (1983)
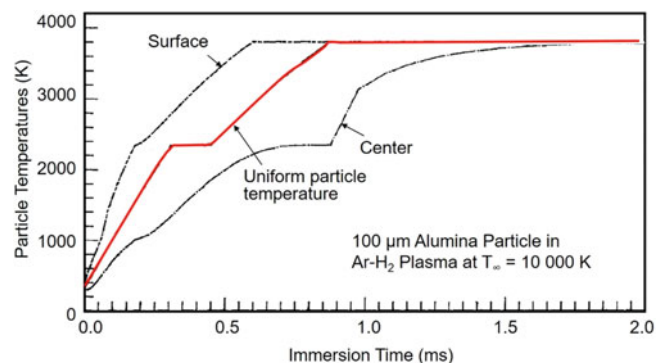


**Fig. 4.32** Temperature history of a 100 μm alumina particle exposed to an argon plasma at 10,000 K, after Chen and Pfender (1982a, b)



**Fig. 4.33** Temperature history of a 100 μm alumina particle exposed to a nitrogen plasma at 10,000 K, after Chen and Pfender (1982a, b)

$H_m$  latent heat of fusion of the particle material
$\kappa_p$  thermal conductivity of the particle material in solid state
$\kappa_\ell$  thermal conductivity of the particle material in liquid state

Typical results reported by Bourdin et al. (1983) given in Fig. 4.31 show the evolution with time of the temperature profile across an alumina and a tungsten particle suddenly immersed into a nitrogen plasma at 10,000 K. Figure 4.31a shows that during the transient heating and melting of an alumina particle with a diameter of 100 μm, the surface temperature of the particle can reach the boiling temperature of alumina (3800 K) before the solid core of the particle is molten. In this particular case the radius of the solid core is 20 μm, at the time its surface reaches 3800 K, corresponding to 6.4% of the mass of the particle still not molten. The effect is a direct consequence of the high heat flux to the surface of the particle and the relatively low thermal conductivity of alumina. Figure 4.31b shows that the situation is quite different for a metallic particle, such as tungsten, where internal temperature gradients during the transient healing and melting of the particle are considerably lower than those observed for alumina.



**Fig. 4.34** Temperature history of a 100 μm alumina particle exposed to an Ar/H$_2$ plasma at 10,000 K, after Chen and Pfender (1982a, b)

Chen and Pfender (1982a, b) reached a similar conclusion in their study of the unsteady heating of small particles in thermal plasmas. Typical results given in Figs. 4.32, 4.33 and 4.34 show the evolution with time of the temperature of the surface and center of a 100 μm diameter. Alumina particle
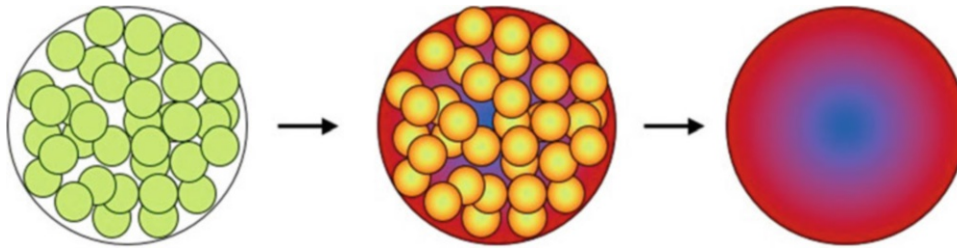
**Fig. 4.35** Schematic representation of the progression of the heating and melting of a porous agglomerated particle

suddenly immersed in a plasma of different compositions at 10,000 K. Superposed on the figures is the corresponding temperature evolution of the same alumina particle assuming a "uniform particle temperature," which is equivalent to assuming an "infinite thermal conductivity" of the particles. The results show for an argon plasma (Fig. 4.32), which is characterized as being a "low-thermal conductivity plasma," the uniform particle temperature assumption is quite acceptable with relatively small internal temperature gradients observed during the melting phase of the particles. The situation is different, however, with a nitrogen or an Ar/H₂ plasma (25 vol. % H₂) (Figs. 4.33 and 4.34) with significant differences observed between the temperatures of the surface and that of the center of the particles. While the assumption of uniform particle temperature is not acceptable in this case, the approach can still be used as a first approximation for the estimation of the time required for the heating and melting of the particle. It should be pointed out that in the case of the treatment of an alumina particle in an argon plasma, the Biot number, defined by Eq. 4.42, was 0.019, while it was equal to 0.16 and 0.28 for the nitrogen and Ar/H₂ cases, respectively. It should be stressed that the phenomenon of internal heat propagation in the particle should be taken into account mostly in the case of low thermal conductivity ceramic particles injected in high thermal conductivity plasmas for which the Biot number is larger than 0.03.

### 4.5.4 Transient Heating and Melting of Porous Spherical Particle

With porous particles such as those obtained by the agglomeration of finer particles, or the atomization of a melt, as shown in Figs. 4.1 and 4.2, the particle can have a void fraction as high as 45% or more with a significant impact on its effective thermal conductivity compared with that of a dense material. Heat propagation phenomenon in such particles during heating and melting steps can be particularly important (Hurevich et al. 2002; Vardelle et al. 1990; Diez et al. 1993). The heat transfer process as schematically represented in Fig. 4.35 involves the transfer of heat through contact points between individual particles in the early stages
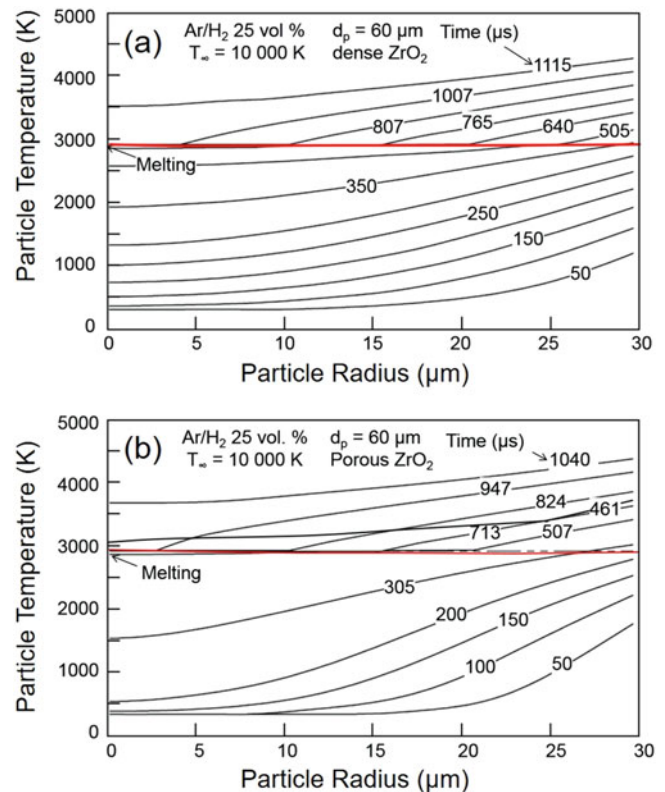


**Fig. 4.36** Transient temperature profiles for a 60 μm diameter ZrO₂ particle in an Ar/H₂ (17 vol.%) plasma at 10,000 K, (**a**) dense particle (**b**) agglomerated particle with 45% void fraction and a mean pore diameter 50 nm Vardelle et al. (1990)

of the heating followed by a gradually improved transfer through the partially melted external shell of the particle. Typical results showing the temperature profile in a 60 μm diameter zirconia (ZrO₂) particle immersed in Ar/H₂ (17 vol. % H₂) plasma at 10,000 K are given in Fig. 4.36. The profiles given in Fig. 4.36a were computed for a fully dense particle, while those in Fig. 4.36b correspond to a porous particle (45% vol.) with a mean pore diameter of 50 nm.

As shown by Hurevich et al. (2002), the effect of porosity is taken into account by reducing the effective thermal conductivity of the bulk material. Experiments have shown, however, that the phenomenon is more complex since the

gas in the pores, or that created by the evaporation of an organic binder in agglomerated particles, must find its way from the particle. This is relatively easy when spraying small particles ($d_p \sim 30$ μm) where the molten shell reaches temperatures beyond 3500 to 4500 K, thus allowing the gas to escape through the low viscosity liquid meniscus (Vardelle et al. 1990) giving rise to the formation of dense spherical droplets, which can be recovered as dense particles once they cool down and solidify. In contrast, larger porous particles ($d \geq 60$ μm) might not have the time to be sufficiently heated to allow the entrapped gas to escape through the molten shell. The collected particles in this case would have residual porosity and could constitute hollow spheres containing unmolten grains of the finer unmolten particles Diez and Smith (1993) and Chang and Khor (1996) reported similar results in a study of heating and melting of agglomerated hydroxyapatite powders. However, in most of these cases, dealing with agglomerated large particles, the powders are treated in a furnace to get rid of the binder material before being used in a plasma spraying operation. It should be pointed out that full densification and melting of powders is not required for the spraying of nanometer-sized agglomerated particles where it is important to limit the heating in order to achieve only partial melting of the powder to protect the nanostructure of the material in the coating (Fauchais et al. 2011).

## 4.6 Particle Vaporization Under Plasma Conditions

### 4.6.1 Basic Mechanism of Particle Vaporization

Particle evaporation under plasma conditions can be either a result of an undesirable side effect during the treatment of powders in a thermal plasma due to the overheating and vaporization of the finer size fractions or an integral part of the process for the synthesis of nanopowders. In the first case, especially for powders with a broad particle size distribution, the treatment will result in the overheating of the fine powder fractions before the large[-size fractions can receive the energy required for their heating and complete melting. Moreover, when processing alloys composed of elements with a wide range of thermophysical properties, the treatment can result in the partial loss of the lighter elements through in-flight vaporization. Processes developed for the synthesis of nanopowders of metals and alloys rely, on the other hand, on the complete vaporization of the precursor in the form of fine powder followed by the condensation of the formed vapor as a fine nanopowder with the required particle size distribution. In either case, it is essential for optimal process control to have a fundamental understanding of the basic



$$Q_{cv} = ha\,(T_o - T_s) \qquad Q_{sr} = \epsilon a \sigma\,(T_s^4 - T_w^4)$$
$$Q_{vr} = \oint \varepsilon_T\,dv$$

particle

Vapor cloud
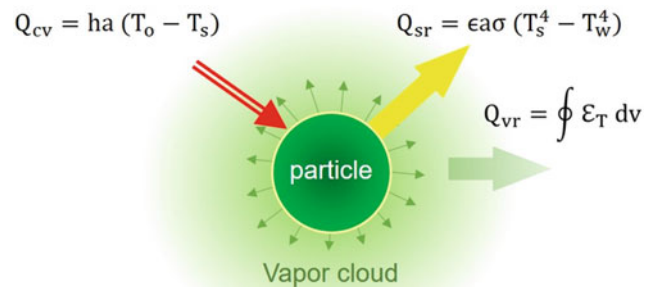
**Fig. 4.37** Schematic representation of the basic phenomena involved during in-flight particle heating, melting and vaporization under plasma conditions

phenomena involved and their impact on process efficiencies and product quality.

A schematic representation of the basic phenomena involved in-flight particle heating, melting, and vaporization of a spherical particle is given in Fig. 4.37. This shows that the particle receives heat from the plasma by conduction and convection, $Q_{cv}$. The particle, in turn, losses heat to the surrounding by radiation from its surface $Q_{sr}$. The net energy received by the particle, given by Eq. 4.23, $Q_n = (Q_{cv} - Q_{sr})$, is responsible for the heating, melting, and eventually the vaporization of the particle material. Since conduction is generally the predominant heat transfer mechanism for particle heating, the analysis given in this section will also be limited to pure conduction for which $Nu = 2.0$. It is important to note, however, that the value of $Q_{cv}$ evaluated on the basis of pure conduction to the particle surface, will be reduced in the presence of particle evaporation due to the local cooling of the boundary layer surrounding the particle by the vapor species liberated at the surface. In the case of metallic particles, the heat transfer to the particle surface is further significantly reduced as a result of the intense volumetric radiation losses emitted from the hot vapor cloud surrounding the particle, $Q_{vr}$.

At equilibrium, depending on the thermophysical properties of the particle and the nature of the evaporated elements, the process can be either mass-transfer or heat-transfer controlled. *Mass-transfer controlled*, in which the evaporation rate is controlled by the diffusion rate of the vapors across the boundary layer, will be favored for non-metallic, low boiling point materials, and materials with a low latent heat of vaporization. *Heat transferred controlled*, on the other hand, in which the particle evaporation rate is controlled by the heat transfer rate, will be the dominating mechanism for metallic materials with a high melting and vaporization temperatures. In the latter case, the particle vaporization rate is given by the following energy balance equation:

$$\frac{dm_p}{dt} = \frac{Q_n}{H_v} \qquad (4.48)$$

where $m_p$ is the mass of the particle and $Q_n$ is the net heat exchange between the plasma and the particle, and $H_v$ is the latent heat of vaporization of the particle material.

### 4.6.2 Effect of Vaporization on Heat Transfer

For an evaporating particle, the vapors liberated at the surface will diffuse through the boundary layer surrounding the particle resulting in the significant cooling of the boundary layer and the corresponding increase of its thickness with the combined effect of reducing the heat flux to the particle. With the further increase of the evaporation rate, the heat transfer coefficients continue to decrease giving rise to a strong non-linearity in the transport equations. According to Chen and Pfender (1982a, b and Chen et al. (1985), the heat received by a spherical particle immersed in a uniform temperature plasma in the absence of evaporation, neglecting radiation exchange from and to the particle, can be written as:

$$Q_o = 2\pi d_p (S_{T\infty} - S_{Ts}) \qquad (4.49)$$

With

$$S_T = \int_{T_0}^{T} \kappa \, dT \qquad (4.50)$$

$T_0$ is a reference temperature, $S_{Ts}$ and $S_{T\infty}$ are the values of the heat transfer potential at the surface of the particle and far away from the particle. The corresponding value of the heat flux to the particle per unit surface area, $q_0$, is inversely proportional to the particle diameter, as given by Eq. 4.51:

$$q_o = \frac{2(S_\infty - S_s)}{d_p} \qquad (4.51)$$

In the presence of evaporation from the surface of the particle, an additional assumption has to be made that the density of the gas phase is considerably lower than that of the condensed phase, and consequently that mass transfer can be treated as quasi-steady processes. The total heat transfer rate, $Q_e$, and the corresponding heat flux values, $q_e$, to the particle surface are given by:

$$Q_e = 2\pi d_p H_v \int_{T_s}^{T_\infty} \frac{\kappa_\infty \, dT}{h - h_s + H_v} \qquad (4.52)$$

$$q_e = \frac{2 H_v}{d_p} \int_{T_s}^{T_\infty} \frac{\kappa_\infty \, dT}{h - h_s + H_v} \qquad (4.53)$$

Dividing Eq. 4.53 by Eq. 4.51 gives:

$$\frac{q_e}{q_o} = \frac{H_v}{(S_\infty - S_s)} \int_{T_s}^{T_\infty} \frac{\kappa_\infty \, dT}{h - h_s + H_v} \qquad (4.54)$$

With the integral being only a function of plasma temperature for a given plasma composition and particle material. Calculations of the heat transfer ratio ($Q_e/Q_0$) for water droplets, alumina, graphite, and tungsten in a pure argon plasma were reported by Chen and Pfender (1982a) using the thermophysical material properties listed in Table 4.6. The results given in Fig. 4.38 show the strongest effect of the evaporation on the heat flux to the particles at high plasma temperatures, and for materials with low latent heat of evaporation such as water.

Chen and Pfender (1982a) developed further their analysis of the quasi-steady evaporation of particles under plasma conditions in order to calculate the evaporation time, $t_e$, of a particle with an initial diameter of $d_{po}$, which they gave as:

$$t_e = \frac{d_{po}^2}{4K} \qquad (4.55)$$

With

$$K = \frac{2 \int_{T_s}^{T_\infty} \frac{\kappa \, dT}{(h - h_s + H_v)}}{\rho_p} \qquad (4.56)$$

**Table 4.6** Thermophysical properties, after Chen and Pfender (1982a)

| Material | Water | Alumina | Graphite | Tungsten |
|---|---|---|---|---|
| $T_s$ (K) | 370 | 3800 | 4100 | 5950 |
| $H_v$ (MJ/kg) | 2.26 | 24.7 | 59.7 | 4.62 |
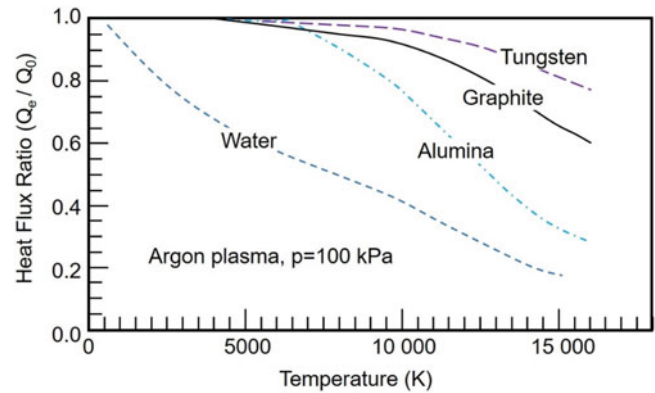


**Fig. 4.38** Effect of evaporation (or sublimation) on the heat flux to a spherical particle for Re = 0, $Q_e$: heat flux in the presence of evaporation, $Q_o$ heat flux in the absence of evaporation, after Chen and Pfender (1982a)
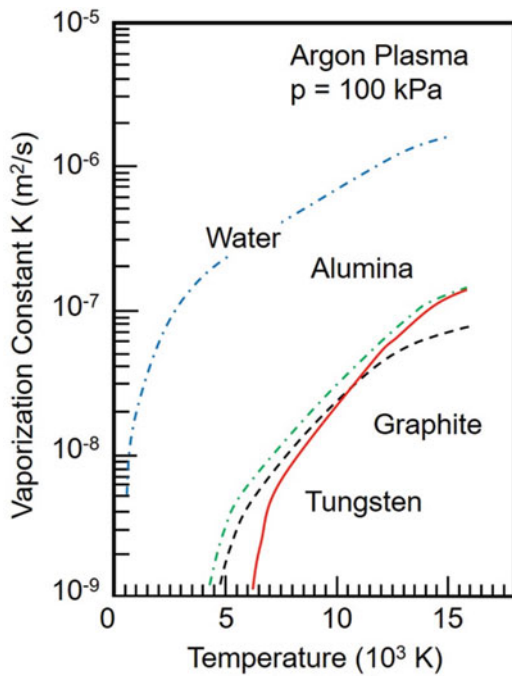
**Fig. 4.39** Vaporization constant for different materials in an atmospheric pressure argon plasma, After Chen and Pfender (1982a)



**Fig. 4.40** Effect of evaporation on heat transfer to a water for Ar, $N_2$, and Ar/$H_2$ 20 vol.% $H_2$ plasmas at atmospheric pressure, after Chen and Pfender (1982a)



**Fig. 4.41** Effect of evaporation on heat transfer to a tungsten particle for Ar, $N_2$, and Ar/$H_2$ 20 vol.% $H_2$ plasmas at atmospheric pressure, after Chen and Pfender (1982a)

It is to be noted that the evaporation time calculated using Eq. 4.55 does not include the time required for the initial heating and melting of the particle and the subsequent heating of t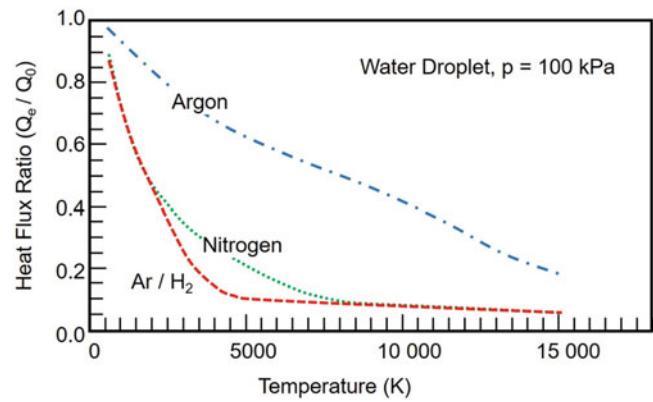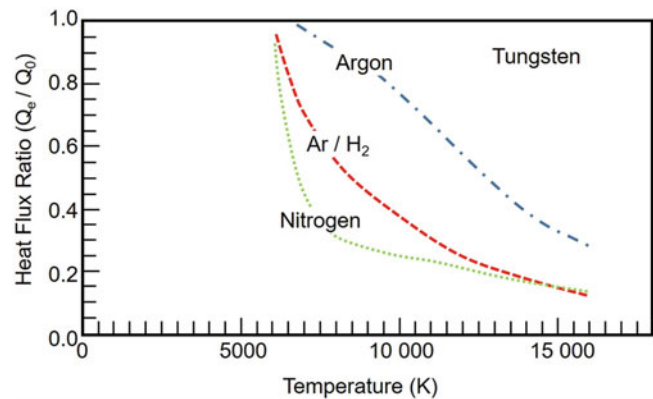he liquid droplet up to its vaporization (boiling) temperature. Eq. 4.55 also shows that, $K$, is a function of the thermophysical properties of the plasma and the particle, and the vaporization time for a given material and plasma system is directly proportional to the square of the initial particle diameter. Variations of the value of $K$ with temperature for atmospheric pressure argon plasma are given in Fig. 4.39 for water, alumina, graphite, and tungsten. According to Eq. 4.55 and using the corresponding values of the vaporization constant, $K$, the vaporization time for a 100 μm water droplet in a 12,000 K argon plasma would be 2.43 ms. Corresponding values for an alumina, graphite or tungsten particles of the same diameter would be 41.5, 60.1, and 50.2 ms, respectively. As mentioned earlier, these values do not include the initial particle heating, melting, and subsequent liquid superheating time to bring the particle temperature to its evaporation (boiling) temperature. Moreover, the heat transfer mechanism involved in these calculations was limited to pure conduction between the plasma and the particle surface.

The effect of the composition of the plasma gas on the evaporation rate of different materials, and subsequently on the ratio ($Q_e/Q_0$) as function of the plasma temperature, was further investigated by Chen and Pfender (1982a). Typical results obtained for water droplets and tungsten particles immersed in an Ar, A/$H_2$ (1:4 molar ratio) and $N_2$ are presented in Figs. 4.40 and 4.41. These show a significant reduction of the ratio of the heat rate to the particle with the increase of the vaporization rate. The effect is more pronounced for an Ar/$H_2$ and $N_2$ plasma compared with that for a pure Ar plasma.

The corresponding vaporization constant, $K$, for these two materials in Ar, Ar/$H_2$ (1:4 molar ratio) and $N_2$ plasmas are given in Fig. 4.42. In contrast to the effect of vaporization on heat transfer, which was observed in Figs. 4.40 and 4.41 to be stronger for materials with a lower latent heat of evaporation, the vaporization constant seems more dependent on the density of the condensed phase (Figs. 4.43 and 4.44).
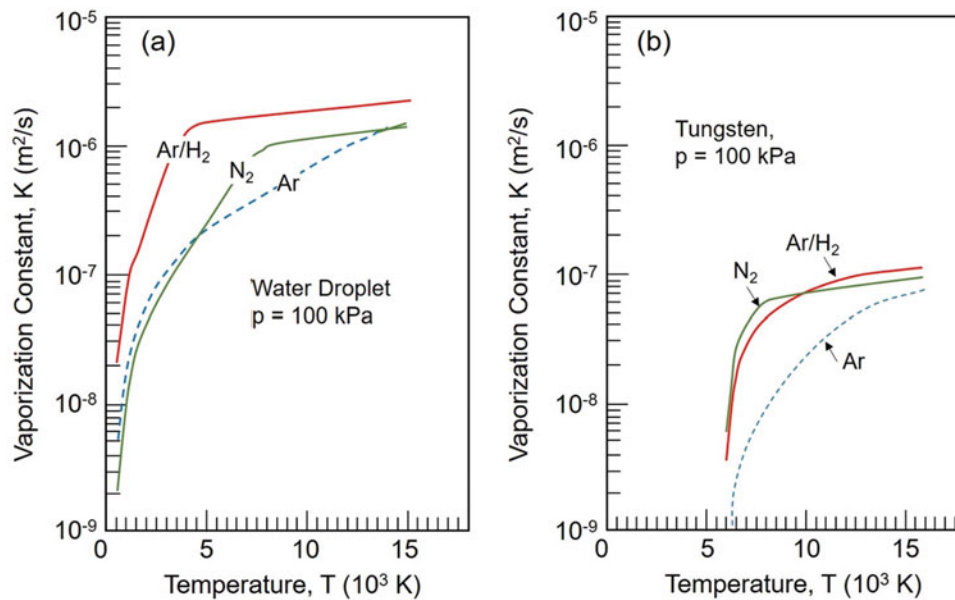
**Fig. 4.42** Effect of the plasma composition on the vaporization constant as function of the plasma temperature for water and tungsten Chen and Pfender (1982a)
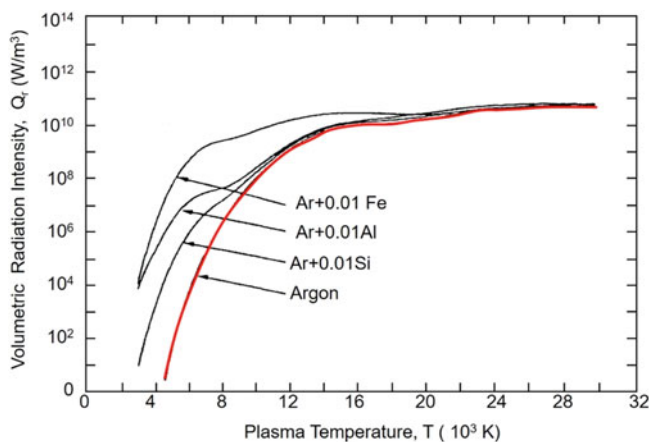


**Fig. 4.43** Volumetric emission for an argon plasma in the presence of 1% molar fraction of different metallic vapors, plasma radius = 1 mm, after Essoltani et al. (1994)
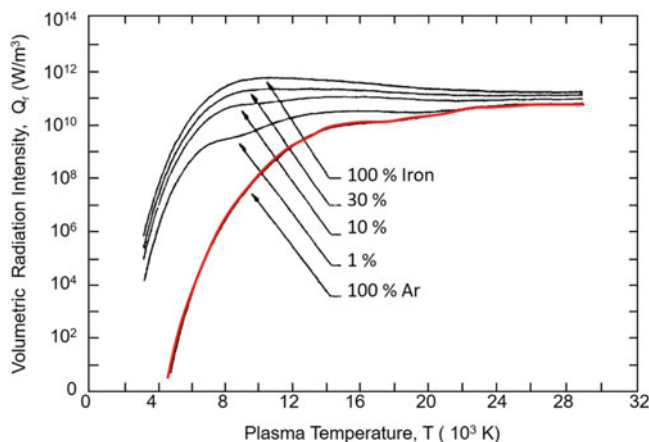


**Fig. 4.44** Volumetric radiation losses for an Ar/Fe plasma as function of temperature and the molar fraction of iron vapor, plasma radius R = 1 mm, after Essoltani et al. (1990)

### 4.6.3  Effect of Radiation on Particle Vaporization

As illustrated in Fig. 4.37, radiation effects can have an impact on particle heating and vaporization through:

- Radiation exchange between the surface of the particle and its surrounding
- Volumetric radiation losses from the vapor cloud surrounding the particle

As mentioned earlier, the heating of the particle through radiation received from the surrounding can generally be negligible. On the other hand, heat losses by radiation from the surface of the particle can be significant, limiting the ability of heating the particle to reach its melting or vaporization temperature, as discussed earlier in Sect. 4.4.3. Chen and Pfender (1982b) integrated in Eqs. 4.52 and 4.53 radiation heat losses from the surface of the particle, giving rise to Eq. 4.57:

$$Q_{sr} = 2\pi d_p H_v \int_{T_s}^{T_\infty} \frac{\kappa_\infty \, dT}{h - h_s + c} \tag{4.57}$$

with

$$c = H_v + \frac{2\pi \, d_p^2 \, \varepsilon \, \sigma_s \, T_s^4}{\frac{dm}{dt}} \tag{4.58}$$

where $h$ is the plasma specific enthalpy at $T$, while $h_s$ is the plasma specific enthalpy at $T_s$. This expression has been deduced assuming that the plasma thermodynamic and transport properties $(h, \kappa)$ are not modified by the vapor diffusion.

Assuming $\left(\kappa/c_p = \overline{\kappa}/\overline{c_p}\right)$ in the boundary layer, Eq. 4.57 applies:

$$Q_{sr} = \frac{H_v}{h - h_s} \; ln\left(1 + \frac{h - h_s}{H_v}\right) 2\pi \, d_p \left(\overline{\kappa}/\overline{c_p}\right)(h - h_s)$$

$$(4.59)$$

Equation 4.57 is equivalent to the introduction of a correction factor $\lambda_c$ to the thermal flux due to the plasma, Borgianni et al. (1969):

$$\lambda_c = \frac{H_v}{h - h_s} \ln\left[1 + \frac{h - h_s}{H_v}\right] \qquad (4.60)$$

Volumetric radiation losses from the plasma surrounding a particle can also result in a significant cooling of the boundary layer and the reduction of the heat transfer rate to the particle. The effect is particularly important for metallic particles since radiative energy losses from the metal vapors under plasma conditions can be important as reported by Cram (1985), Essoltani et al. (1990), Essoltani et al. (1991), Essoltani et al. (1994), and Vardelle et al. (1996). The effect is illustrated in Fig. 4.46, after Essoltani et al. (1990) shows that in the temperature range from 3000 to 8000 K the radiation losses of the vapor in the presence of only 1% molar of concentration of metallic vapors (Si, Al or Fe) can be several orders of magnitude higher than that of pure argon plasma. In this figure the effective radiation (including self-absorption) has been calculated for volume element of 1 mm in radius. The effect increases rapidly with the increase of the metal vapor concentration as illustrated in Fig. 4.47 for the Fe/Ar system (Essoltani et al. 1994). A detailed discussion of the effect of metal vapors on volumetric radiation losses under plasma conditions can be found in Boulos et al. (2021), Handbook of thermal plasmas, Part I, "Fundamentals of thermal plasmas," Chap. 8, "Plasma radiation transport."

A study of the effect of the radiative energy losses from the vapor surrounding an evaporating particle on the heat transfer rate to the particle was reported by Essoltani et al. (1993). The proposed transient model follows the development of the thermal boundary layer surrounding a single, 100 μm diameter, spherical iron particle suddenly immersed in a pure argon plasma at atmospheric pressure and a temperature of 10,000 K. The particle was assumed to be at the boiling temperature of iron, 3000 K and the relative velocity between the plasma and the particle was 10 m/s. The model is based on the solution of the corresponding 2-D continuity, momentum, energy, and mass transfer equations. The
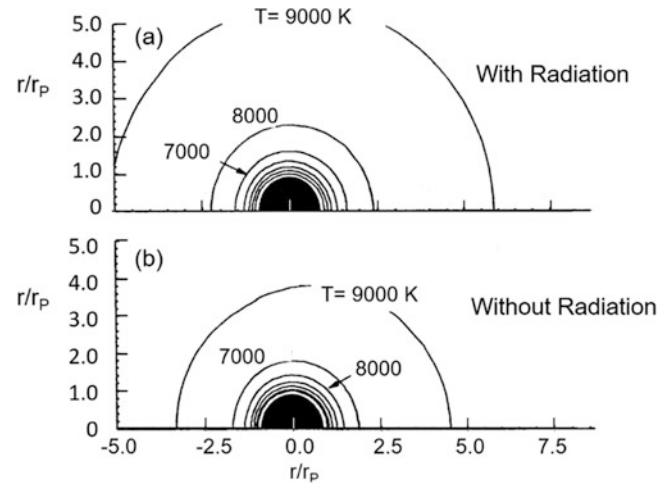


**Fig. 4.45** Temperature contours around a 100 μm iron particle immersed in argon plasma at 10,000 K with a relative velocity of 10 m/s, (**a**) Considering radiation from the iron vapor and (**b**) neglecting radiation effects, after Essoltani et all (1993)

computation was limited to a short time period of the order of 100 μs, over which the particle diameter was assumed to be constant.

Typical results showing the temperature contours around the particle are given in Fig. 4.45. The results given in the upper part of the figure (Fig. 4.45a) were obtained taking into account radiation losses from the iron vapor surrounding the particle. The corresponding isocontours obtained neglecting radiation effects are given in the lower part of the figure (Fig. 4.45b). The importance of the radiative cooling of the plasma close to the surface of the particle is clearly demonstrated by the displacement of the high temperature isotherms away from the surface of the particle giving rise to smaller temperature gradients and lower heat transfer rates to the particle. Due to convective effects, the vapor concentration and temperature profiles in the boundary region surrounding the particle on the upstream and downstream side of the particle are different as shown in Fig. 4.46. The time-dependent variation of the temperature profile at 90° from the stagnation point of the flow ($\theta = 90°$) as function of the reduced radius ($r/r_p$) is given in Fig. 4.47a. The corresponding variation with time of the average Nusselt number over the entire surface of the particle is given in Fig. 4.47b. This shows a rapid drop of the Nu, from its pure conduction value of 2.0 to almost 0.6 in less than 10 μs due to the establishment of an iron vapor-rich boundary layer surrounding the particle responsible for the significant local cooling of the plasma due to radiative effects.
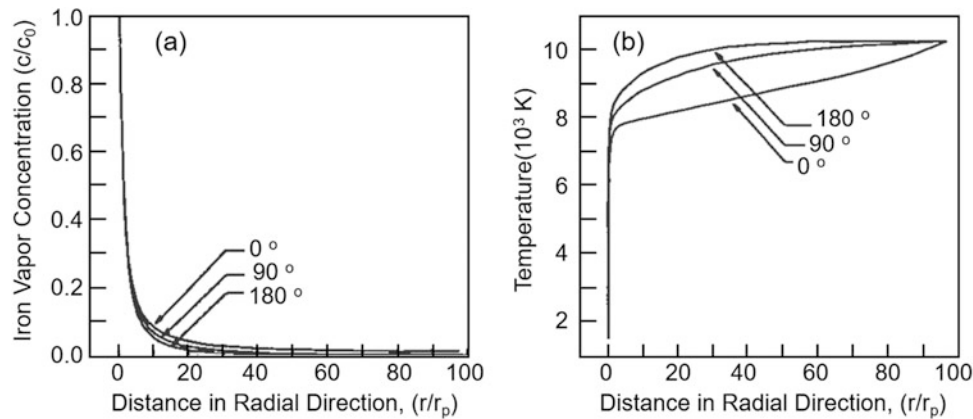
**Fig. 4.46** (**a**) Local iron vapor concentration and (**b**) temperature radial profiles at different angles from the stagnation point of the flow ($\theta = 0\,°$) at t = 1 µs, after Essoltani et al. (1993)
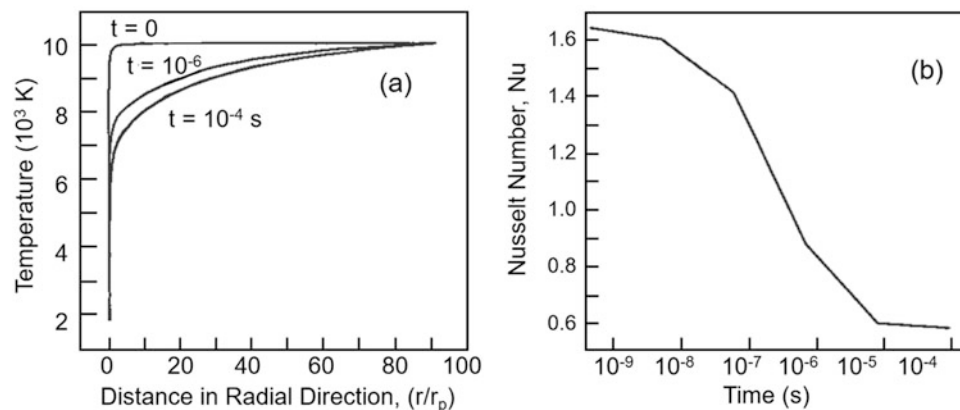


**Fig. 4.47** (**a**) Transient temperature profiles at $\theta = 90\,°$, and (**b**) Corresponding variation with time of the Nusselt number, after Essoltani et al. (1993)

### 4.6.4 Effect of Mass Transfer and Chemical Reactions

In the case of metal particles injected in a plasma flow in an open-air atmosphere, such as in atmospheric plasma spraying (APS) operations, particle vaporization can be controlled by transport process involving the diffusion of oxygen from the plasma to the particle and chemical process leading to homogeneous oxidation reaction, which consumes the metal vapor and thereby increases the evaporation rate from the liquid surface. Above a critical value of oxygen partial pressure, the flux of oxygen molecules toward the particle is greater than the counter flux of metal vapor away from the particle. A solid or liquid oxide layer may then form on the particle surface reducing significantly the rate of vaporization.

The effect of chemical reaction on the vaporization of metallic particles was demonstrated by Vardelle et al. (1996), comparing the evaporation rates of iron particles injected into an $Ar/H_2$ plasma jet in an inert atmosphere, with that in the presence of ambient air. When operating in

an inert atmosphere, the vapor atoms/molecules produced by particle vaporization diffuse without reacting through the boundary layer surrounding the molten metal droplet, reducing the heat transfer rate to the droplet, as discussed earlier in Sect. 4.6.2, "Effect of vaporization on the heat transfer to a spherical particle," and Sect. 4.6.3, "Effect of radiation on particle vaporization." In the presence of oxygen in the ambient atmosphere, the counter diffusion of oxygen towards the surface of the evaporating droplet and its reaction with the metal vapor results in a decrease of the metal vapor concentration at the surface of the particle, which helps to sustain the higher rate of the evaporation. The proposed mechanism was supported by measurements of the radial density profile of iron atoms at a distance of 80 mm from the plasma jet exit nozzle, for an $Ar/H_2$ (25 vol.% $H_2$) plasma jet in which iron particles (15–45 µm) are injected at a rate of 50 g/h. The results given in Fig. 4.48. show that with air as ambient gas the density of iron atoms in vapor phase is almost two orders of magnitude higher than that measured in an argon atmosphere.
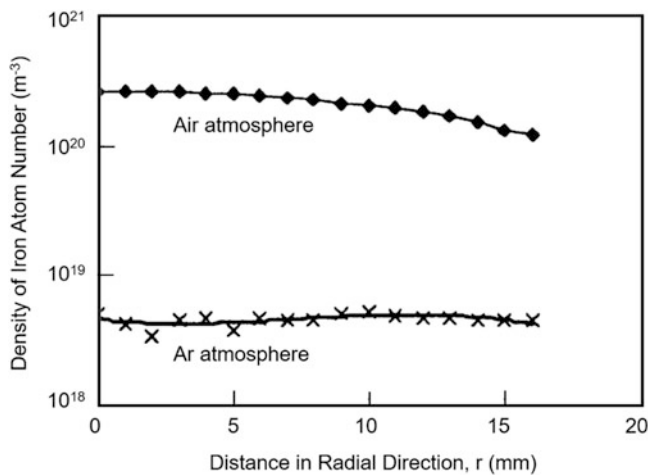
**Fig. 4.48** Radial profiles of iron atom distribution in an Ar-H$_2$ plasma jet in which iron particles are injected, issuing into air or argon atmosphere, after Vardelle et al. (1996)
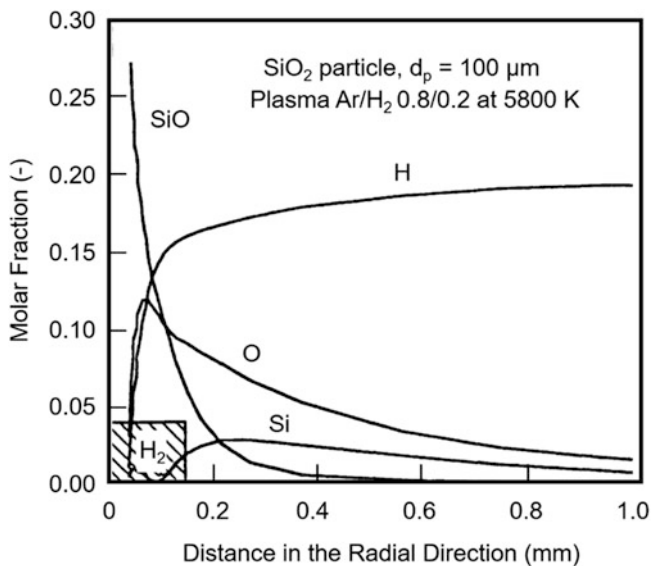


**Fig. 4.49** Evolution of the molar fraction of the different chemical species around a 100 μm diameter SiO$_2$ particle in an Ar/H$_2$ (20 vol. %) plasma at 5800 K, calculated according to data of Humbert (1991)

In the case of nonmetallic particles, particle evaporation can also be associated with chemical decomposition of the particle material, giving rise to more complex mechanisms controlling the evaporation rate. A typical result is illustrated in Fig. 4.49 after Humbert (1991) for the evaporation of SiO$_2$ particles, 100 μm in diameter, immersed in Ar/H$_2$ plasma (20 vol. % H$_2$) at 5800 K. The results given in this figure show that close to the particle surface, the vapor comprises mostly of SiO, which is further reduced by H atoms as the vapor diffuses away from the particle surface.

## 4.7 Chemical Reactions and Melt Circulation

### 4.7.1 Diffusion Controlled Reaction

When the partial pressure of the reacting gas in the bulk of the hot gas surrounding a particle reaches a specific value, defined as the critical pressure, the flux of reacting species toward the surface of the droplet exceeds the counter flux of metal vapor, and a liquid or solid oxide, nitride or carbide layer (depending on the hot gas forming gas composition and ambient atmosphere) forms on the surface of the droplet. Typical values of the critical pressure of oxygen for an oxidation reaction can be calculated from:

$$p_{O_2\,max} = \frac{p_i}{\alpha_s\, h_{O_2}} \sqrt{\frac{RT}{2\pi M_i}} \qquad (4.61)$$

where $\alpha_s$ is the number of g-atoms of metal vapor required to combine with 1 mole of oxygen at the surface of the droplet, $h_{O_2}$ is the mass transfer coefficient of oxygen (m/s), $M_i$ is the atomic mass of the metal (kg) and $p_i$ is the partial pressure of the vapor.

Under typical plasma spraying conditions, oxidation of the sprayed metal can take place either in the vapor phase surrounding the droplet, or at the surface of the droplet. In the latter case the formed oxide layer can result in a considerable reduction of the evaporation rate from the droplet surface. The effect is strongly dependent on the particle diameter, as illustrated in Fig. 4.50, for iron particles of diameters 40 and 80 μm, injected at 10 m/s into an Ar/H$_2$ DC plasma jet (conditions same as that of Fig. 4.48). The results are given in terms of molar ratio of the evaporated to the oxidized fraction of the iron particle as function of its axial position on its trajectory. As expected the smaller particles, $d_p = 40$ μm, evaporate at a faster rate compared to the larger 80 μm particles, with comparable in-flight oxidation. This implies that if the trajectory of the 40 μm particle is optimum, the 80 μm particle will cross earlier the jet and thus is less heated. This results in a much lower evaporation in the latter case with a strong oxidation, while the opposite is true for the smaller particle.

At the end of the trajectory of the particle in the plasma, the composition of its surface depends on its temperature history, and the reactive species present in the plasma, provided that they can reach the particle surface. Thermodynamic equilibrium calculation can serve for the calculation of the chemical composition of the particles prior to their impact on the substrate. While the plasma conditions often deviate from equilibrium, the knowledge of phases which are thermodynamically stable under given conditions, and how they compare with those present in real systems, is very
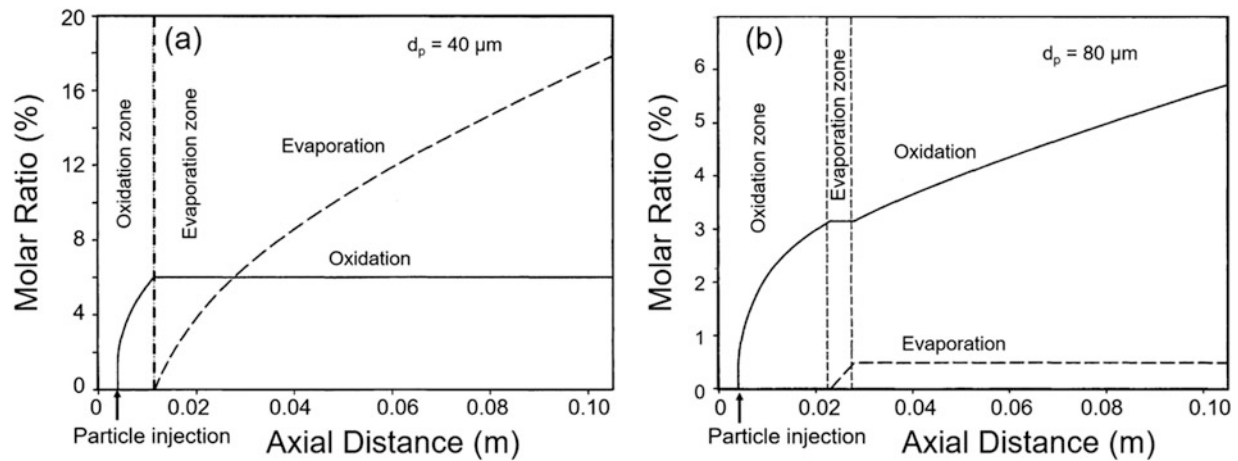
**Fig. 4.50** Molar ratio of evaporated and oxidized fractions of an iron particle along its trajectory in an Ar/H₂ plasma jet. (**a**) $d_p = 40$ μm, (**b**) $d_p = 80$ μm, after Vardelle et al. (1996)

informative. This has been demonstrated, for example, for the oxides in plasma-sprayed chromium steel (Volenik 1997).

The next step is to calculate the diffusion phenomena occurring at the interfaces, diffusion of the reactant through the shell formed at the particle surface (in liquid or solid state), diffusion of gaseous reaction products formed (if any) through the shell and then through the boundary layer (see the shrinking core model described Asaki et al. (1974), Arnauld et al. (1985), and Amouroux et al. (1985)). The diffusion coefficients can be strongly affected by the expansion mismatch between the non-reacted particle core and the reacted shell formed around the core, which can be easily broken if it is in the solid phase.

A few examples of oxidation reactions can be found in the following references: Essoltani et al. (1990), − Vardelle et al. (1996), Li et al. (1995), Vardelle et al. (2002), Volenik et al. (1997), Vardelle et al. (1998), Espié et al. (2001), Volenik et al. (2003), Espié et al. (2005), Seyed et al. (2005). Pertinent references for other reactive systems, such as TiC + Ti, SiC + Si, W + $W_xC_y$, Mo + $MoC_2$, NiCr/Ti + TiC + $Cr_xC_y$, FeCrAlY + $Cr_xFe_y$ + $Fe_xC_y$, Mo + $MoSi_2$, and Ti + $TiB_2$ can be found in Smith and Matasin (1992), Dallaire (1992), Jiang et al. (1994), Eckardt et al. (1994), Fauchais et al. 1997a, b), Dai et al. (1998), Fan and Ishigaki (1998), Denoirjean et al. (2003)).

### 4.7.2 Reactions Taking Place Between Condensed Phases

In this case, the basic reactants are in the solid phase either as cladded or agglomerated particles (Dallaire 1992; Borisov and Borisova 1993; Shaw et al. 1994; Deevi et al. 1997; Haller et al. 2004; Bach et al. 2001; Haller 2006) (see Fig. 4.51). The most common cladded particle is the Ni–Al where an Al core is surrounded by a Ni shell. Upon melting, Al reacts with the Ni creating intermetallic species such as
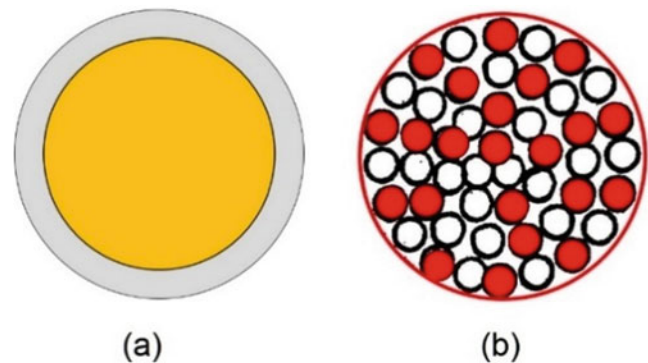


**Fig. 4.51** (**a**) Cladded or (**b**) agglomerated, composite particles, which can be used for SHS plasma spraying Borisov and Borisova (1993)

$Ni_3Al$, NiAl. The same holds for agglomerated particles of Ti and C, for example, (Dallaire 1992). Hot gases heating of the particle triggers the reaction and initiates the self-propagation high temperature synthesis (SHS). The reaction depends strongly on the size of agglomerated particles and the possibility to heat the agglomerated particles without destroying the agglomerates by the produced gas expansion. As the speed of SHS is typically between 1 and 150 mm/s, the SHS reaction propagation is not necessarily completed during the flight time of the particles and may proceed after their impact resulting in very dense and hard coatings (Haller 2006).

Numerous coatings have been produced using the following approach:

- Transition metal/non-metal refractory compounds with mixtures of Cr and SiC or $B_4C$, Ti and SiC or $B_4C$ or $Si_3N_4$ producing coatings with silicides, carbides, borides, which show excellent resistance to wear (Cliche and Dallaire 1991; Dallaire 1992; Dallaire and Cliche 1992; Borisov et al. 1986; Legoux and Dallaire 1993; Shaw et al. 1994)
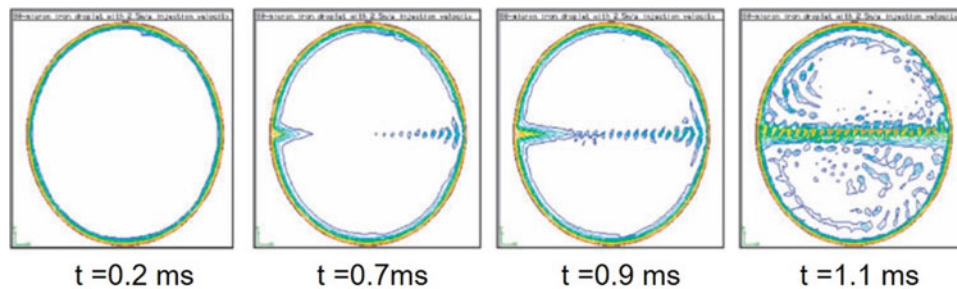
**Fig. 4.52** Time-resolved modeling of internal convection and oxide penetration by a spherical vortex of Hill in a molten iron particle Espié et al. (1999)

- Copper-TiB$_2$ coatings starting from agglomerated particles of Ti-bronze and boron, the TiB$_2$ particles in coatings increase considerably the hardness of copper (Legoux and Dallaire 1993)
- TiB$_2$ or TiC particles in ferrous matrices to increase their hardness and wear resistance (Dallaire and Champagne 1984; Cliche and Dallaire 1991; Dallaire and Cliche 1992)
- Al and metal oxides to produce intermetallic compounds with aluminum particles (Bach et al. 2001)

### 4.7.3  Reactions Controlled by Convection Within Liquid Phase

Such reactions within droplets occur only in DC plasma jets as well as in wire-arc spraying where the shear stress at the surface of the molten droplet created by the large velocity difference between the molten particle in flight and the plasma flow induces a convective motion within the droplet. The phenomena is observed when the ratio of the kinematics viscosities of the plasma and the droplet is greater than 50 and the Reynolds number of the flow relative to droplet greater than 20 (Neiser et al. 1998). The motion inside the droplet can be represented by a Hill vortex that is an inviscid axi-symmetric vortex (Espié et al. 1999). For a low carbon 60 μm iron droplet in a DC Ar–H$_2$ plasma jet, time-dependent computations performed by using a commercial code, FIDAP7-62, dedicated to the materials processing field [FIDAP code], indicated the formation of internal convection motion in the molten iron particle with oxide penetration inside the droplet caused by the spherical Hill's vortex as shown in Fig. 4.52.

The internal circulation in the liquid metal droplet continuously sweeps fresh liquid to its surface and makes it available for oxidation. As a result of this circulation, portions of the outer layer or of the dissolved oxygen at the droplet surface are entrained and transported to the core of the droplet. For a low-carbon iron particle, the oxide formed at the surface is liquid Fe$_x$O. Liquid iron and liquid Fe$_x$O are not miscible due to the significant difference in their surface tension (1778 mJ.m$^2$ for pure iron and 585 mJ. m$^2$ for the wüstite Volenik et al. (1997)). Upon cooling,
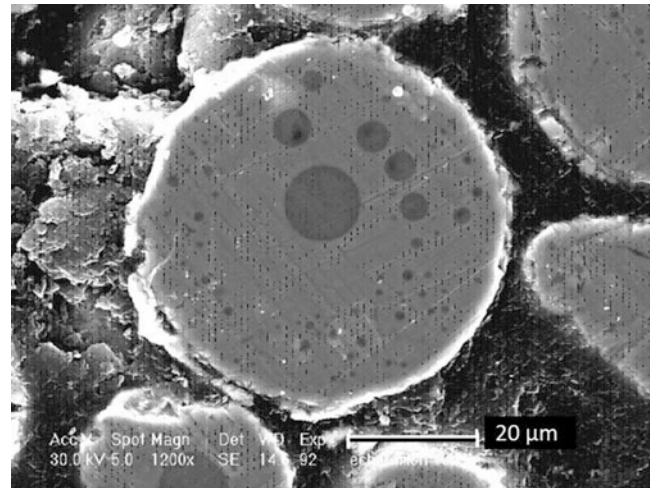


**Fig. 4.53** Cross sections of a low carbon steel particle collected at z = 100 mm after its flight in a DC plasma jet: Ar 50 slm, H$_2$ 10 slm, I = 500 A, nozzle i.d. 7 mm. SEM analysis at 30 keV. Scale 20 μm Espié et al. (1999)

both phases separate and spherical Fe$_x$O nodules are formed within the solidified particle, as shown in Fig. 4.53. Such recirculating flow within the droplet gives rise to an increase of the oxygen content in the solidified particle compared with that estimated by assuming a pure diffusion model Espié et al. (1999). For the iron particles shown in Fig. 4.53, the captured FeO corresponding to a mass percentage is 15 wt. %, while diffusion calculations estimate the Fe$_2$O$_3$ and Fe$_3$O$_4$ concentration to be less than 3 wt. %. The oxide shell formed at the surface of particles, with no inside convective movement, is made of Fe$_2$O$_3$ and Fe$_3$O$_4$. Such oxides are observed in the thin shell surrounding the particle formed at the end of the particle trajectory when the particle velocity is about the same as that of the surrounding plasma plume (no more convective effect). The same effect was observed with stainless steel particles plasma sprayed with Ar–H$_2$ plasma forming gas (Seyed et al. 2005).

Similar results have been observed when spraying Ti-6Al-4V particles in a DC nitrogen plasma under controlled atmosphere or in ambient air. TiN and TiO$_2$ contaminants are formed, in the particles with significantly less TiO$_2$ in controlled atmosphere spraying (Ponticaud et al. 2001).

### 4.7.4 Nano- and Micrometer-Sized Particles and Coating Structures

Over the past three decades, the interest for developing and studying nanostructured coatings has grown from about 300 peer-reviewed published in the 1980s to more than 2000 in the 1990s and about 28,000 in the last decade (Fauchais et al. 2011). This was mostly motivated by the superior properties of nanostructured coatings compared with those where the structure is micrometer-sized. Reducing the scale of the coating structure down to the nanometer level gives rise to an increased strength, improved toughness, and increased coefficient of thermal expansion while reducing apparent density and elastic modulus and lowering apparent thermal conductivity, among other numerous potential improvements (Gell 1995). Among the thermal routes, plasma spraying micrometer-sized particles, essentially ceramics, made of agglomerated nanometer sized particles is a possible way. Figure 4.54a (Lima and Marple 2008) shows a spray-dried "nanostructured" agglomerated $Al_2O_3$–13 wt.% $TiO_2$ (alumina–titania) powder (Nanox S2613S, Inframat Corp.,

Farmington, CT, USA). Examining the microstructure of these particles at higher magnification (Fig. 4.54b), it is possible to observe that the agglomerate is composed of individual particles varying from about 15 to 300 nm.

Complete melting of such particles during conventional plasma spraying operation will result in a complete loss of their initial nano-structure. Obviously, the spraying parameters have to be optimized to produce conditions (particle temperatures and velocities) that are limited to the partial melting of the agglomerates (to avoid the complete loss of the nanostructure) while maintaining a sufficiently high degree of melting to ensure effective deposition on the substrate and the formation of so-called nanozones (Lima et al. 2007). One of the critical goals of parameter optimization is to control the density of nanozones, that is, the density of the semi-molten nanostructured agglomerates embedded in the coating microstructure. This is achieved by finding the conditions needed to adjust the amount of the molten part of each semi-molten particle that penetrates into the capillaries (i.e., the non-molten particle core) of the agglomerates (Fig. 4.55) during flight within the thermal spray jet and/or at impact on the substrate surface and subsequent
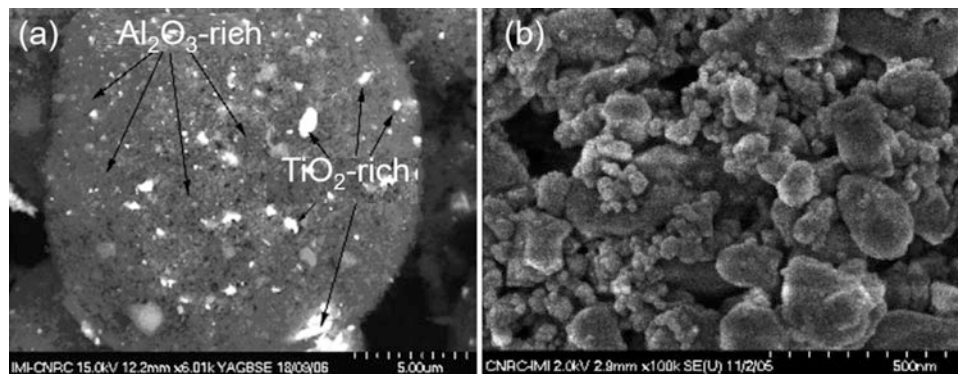


**Fig. 4.54** (**a**) Spray-dried agglomerated $Al_2O_3$–13 wt. %$TiO_2$ particle. (**b**) Higher magnification view showing the "ultra-fine" character of the agglomerate Lima and Marple (2008)
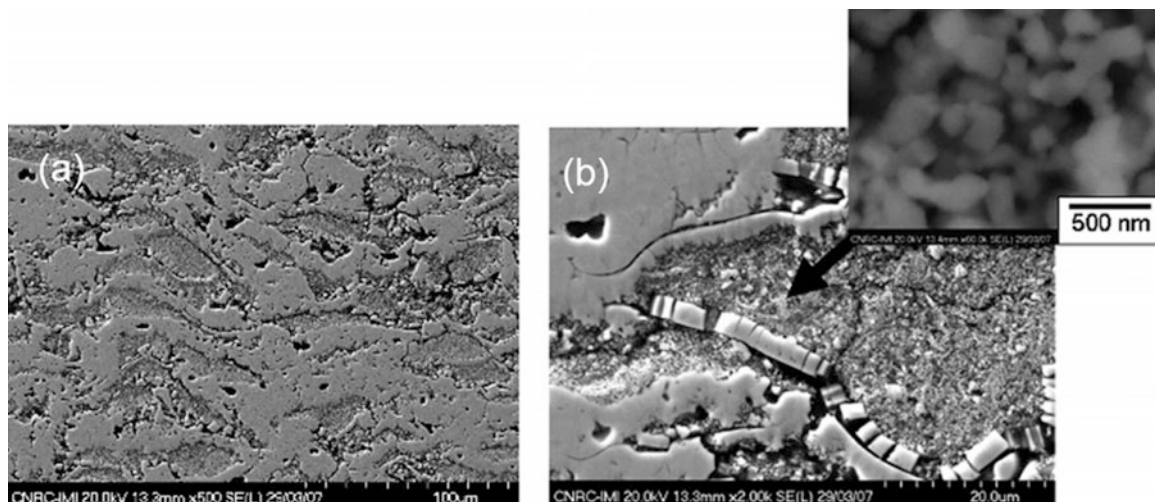


**Fig. 4.55** (**a**) Plasma-sprayed coating (cross-section) engineered from the nanostructured-agglomerated YSZ particles. (**b**) High magnification view showing a semi-molten nanostructured agglomerate (porous nanozones) embedded in the coating microstructure Lima and Marple (2008)

re-solidification. It is important to point out Fauchais et al. (2011) that by introducing porous or dense nanozones throughout the coating microstructure it is possible to engineer coatings with very different and even opposite properties for a variety of purposes. For example, for thermal barrier and abradable seal applications, the presence of porous nanozones is paramount. On the other hand, for anti-wear applications, dense nanozones are absolutely required to induce high levels of wear resistance. The main technique employed for optimizing the spray parameters to engineer coatings produced from nanostructured-agglomerated particles is in-flight particle temperature and velocity monitoring. Moreover, the use of large agglomerates is paramount to engineer architectures that exhibit porous nanozones embedded in the coating micro-structure. For more details, see Lima and Marple (2008), Fauchais et al. (2011).

## 4.8 Summary and Conclusions

Three-dimensional simulations with full coupling between a single particle and gas flow, employing a Lagrangian particle-tracking frame coupled with a steady-state gas flow, have been developed to examine particle motion and heat transfer. These models, when necessary, are compressible and consider the effect on particles of compression and expansion waves. Since the 1990s' models have shown the importance of the different corrections adopted to the process for flames, HVOF or HVAF, D-Gun, and plasma spraying processes: high temperature gradients, particle evaporation or vaporization, rarefaction effect (Knudsen effect), shock waves, supersonic flow effect, such models have shown the drastic influence of the particle injection (position, velocity vector) on its velocity and temperature at impact. Different effects such as loading effect, particle morphology, and shape have been considered. However, the way the particle velocity vector distribution at the injector exit is calculated is still in its infancy in spite of its drastic influence on the particle treatment within the hot or cold gas flow. The first studies of the interaction between hot gas flows and a liquid (solution or suspension spraying) have also been presented; this technique is very promising for the deposition of finely or nanostructured coatings with thicknesses between a few micrometers and hundreds of them.

## Nomenclature

Units are indicated in parentheses; when no units are indicated, the parameter is dimensionless.

## Latin Alphabet

| | |
|---|---|
| $a$ | accommodation coefficient, Eq. 4.22 |
| $a_i$ | sound velocity (m/s) |
| $a_p$ | surface area of particle $\left(a_p = \pi\, d_p^2\right)$ (m²) |
| $A_p$ | particle projected surface area perpendicular to the flow ($A_p = \pi d_p^2/4$) (m²) |
| Bi | Biot number ($Bi = \kappa/\kappa_p$) |
| $c$ | molar density of the bulk gas (mol/m³) |
| $C$ | circularity of a particle, Eq. 4.4 (-) |
| $C_D$ | drag coefficient, Eq.4.16 ($F_D/a_p$)/($0.5\rho v^2$) |
| $c_i$ | mass fraction of metal vapor at the location i |
| $c_{ps}$ | specific heat of the particle |
| $c_{pi}$ | specific heat at constant pressure in the state i (J/kg.K) |
| $c_{vi}$ | specific heat at constant volume in the state i (J/kg.K) |
| $d_d$ | drop diameter (m) |
| $d_l$ | drop or liquid jet diameter (m) |
| $d_p$ | particle diameter (m) |
| $d_{pp}$ | equivalent particle perimeter diameter, Eq. 4.1 (m) |
| $d_{pa}$ | equivalent particle projected area diameter, Eq. 4.2 (m) |
| $d_{pv}$ | equivalent particle volume diameter, Eq. 4.3 (m) |
| $d_{st}$ | Stokes diameter, Eq. 4.6 (m) |
| $D_{vg}$ | diffusion coefficient of metal vapor through the surrounding gas (m²/s) |
| $F_B$ | Basset history term (N) |
| $F_c$ | Coriolis force (N) |
| $F_b$ | body force per unit particle mass (N) |
| $F_d$ | force related to the pressure jump in the detonation wave $\left(F_d = \frac{\pi\, d_p^2}{4}\Delta p\right)$ (N) |
| $F_D$ | drag force exerted by the fluid on the particle (N) |
| $F_g$ | gravity force (N) |
| $F_i$ | inertia force ($m_p \cdot \gamma_p$) (N) |
| $F_p$ | pressure gradient force (N) |
| $F_S$ | surface tension force (N) |
| $F_T$ | thermophoresis force (N) |
| $g$ | gravitational acceleration (g = 9.81 m/s²) |
| $h$ | heat transfer coefficient (W/m²·K) |
| $h_g$ | specific enthalpy (J/kg) |
| $h'_i$ | specific enthalpy of the plasma calculated at i (J/kg) |
| $I$ | arc current (A) |
| $Kn$ | Knudsen number ($Kn = \lambda/dp$) |
| $k_d$ | mass transfer coefficient (m/s) |
| $L$ | mixing length in turbulent model (m) |
| $m_{cg}^o$ | carrier gas mass flow rate (kg/s) |
| $m_p$ | particle mass (kg) |
| $M$ | molecular weight (kg/mol) |
| $Ma$ | mach number (Ma = $v_g/a_g$) |
| $N_{max}$ | maximum molar flux of vaporization from a droplet (m²/s) |
| $Nu$ | Nusselt number ($Nu = hd/\kappa$) |
| $N_v$ | molar flux of vapor (mol/m²·s) |
| $Oh$ | Ohnesorge number $\left(Oh = \mu_l/\sqrt{\rho_l \times d_l \times \sigma_l}\right)$ |
| $p$ | total pressure (Pa) |
| $p_i$ | partial pressure of species i (Pa) |
| $p_o$ | saturation vapor pressure of a liquid (Pa) |
| $P$ | torch power (kW) |
| $P_l$ | splat parameter (m) |
| $P_{eff}$ | torch effective power (kW) |
| $Pr$ | Prandtl number ($Pr = \mu \cdot c_p/\kappa$) |
| $P_p$ | Perimeter of the projected image of the particle (m) |
| $q$ | heat flux (W/m²) |
| $Q$ | heat transferred to a particle (W) |
| $Q_{cv}$ | heat transferred to a particle by conduction and convection (W) |
| $Q_{sr}$ | heat lost from the surface of the particle by radiation to surrounding (W) |
| $Q_{vr}$ | volumetric radiation losses emitted from the hot vapor cloud (W) |
| $Q_n$ | Net energy received by the particle, Eq. 4.23 (W) |
| $r$ | plasma or particle radius (m) |
| $r_d$ | liquid droplet radius (m) |
| $r_s$ | initial liquid drop radius (m) |
| $R$ | plasma torch internal or particle radius (m) |

$R'$      universal ideal gas constant, ($R' = 8.32$ J/K · mol)
$Re$      Reynold's number, ($Re = \rho\, u_R d_p/\mu$)
$R_{inj}$      internal radius of injection tube (m)
$S$      cross section of injection tube (m$^2$)
$S_T$      heat conduction potential, Eq. 4.50 (W/m)
$Sc$      Schmidt's number ($Sc = \nu/D_{v,g}$)
$Sh$      Sherwood's number, ($Sh = k_d.d_p/D_{v,g}$)
$St$      Stokes number ($St = \rho_p\, d_p^2\, v_p/\mu_g l_{BL}$)
$Ste$      Stephan's number; ($Ste = c_{pi}(T_m - T_s)/\Delta H_m$)
$t_d$      drop fragmentation time (s)
$t_r$      time of flight of particles (s)
$t_s$      vaporization time (s)
$T_a$      ambient temperature (K)
$T_f$      mean film temperature, Eq. 4.18 ($T_f = (T_s + T_\infty)/2$) (K)
$T_s$      particle surface temperature (K)
$T_\infty$      free stream plasma temperature (K)
$U$      mean arc voltage (V)
$U(t)$      transient arc voltage (V)
$u$      gas velocity component in the axial direction (m/s)
$u_p$      particle velocity component in the axial direction (m/s)
$u_R$      relative velocity between the particle and its surrounding (m/s)
$u_t$      terminal settling velocity (m/s)
$v$      gas velocity component in the radial direction (m/s)
$v_p$      particle velocity component in the radial direction (m/s)
$V$      volume (m$^3$)
$V_p$      particle volume (m$^3$)
$V_s$      liquid drop volume (m$^3$)
$w_s$      work resulting from the drag force (J)
$We$      Weber number $\left(We = \rho_g u_r^2 d_l/\sigma_l\right)$

## Greek Alphabet

$\alpha_p$      thermal diffusivity of the particle material ($\alpha_p = \kappa_p/\rho_p c_{ps}$)
$\alpha_l$      thermal diffusivity of the molten particle material ($\alpha_l = \kappa_l/\rho_l c_{ls}$)
$\alpha_s$      atoms of metal vapor required to combine with 1 mole of oxygen
$\delta$      boundary layer thickness (m)
$\Delta E_s$      variation of surface energy (J)
$\Delta H_m$      latent heat of fusion (J/kg)
$\Delta H_v$      latent heat of vaporization (J/kg)
$\varepsilon$      particle emissivity (integrated over all wave lengths)
$\phi(r)$      function representing temperature, enthalpy, velocity
$\gamma$      specific heat ratio ($\gamma = c_p/c_v$)
$\gamma_p$      particle acceleration (m/s$^2$)
$\eta_{th}$      torch thermal efficiency (%)
$\kappa$      thermal conductivity of the fluid (W/m K)
$\kappa_p$      thermal conductivity of the particle (W/m K)
$\overline{\kappa}$      mean integrated thermal conductivity, Eq. 4.34 (W/m K)
$\lambda$      plasma mean free path (m)
$\mu$      dynamic viscosity (Pa·s)
$\nu_{cg}$      carrier gas velocity (m/s)
$\nu$      kinematic viscosity ($\nu = \mu/\rho$) (m$^2$/s)
$\rho_g$      gas mass density (kg/m$^3$)
$\rho_o$      fluid density or specific mass (kg/m$^3$)
$\rho_p$      particle density or specific mass (kg/m$^3$)
$\sigma$      droplet surface tension (N/m)
$\sigma_s$      Stephan–Boltzmann constant ($\sigma_s = 5.670 \times 10^{-8}$ W/m$^2$·K$^4$)
$\sigma_x$      standard deviation
$\xi$      ratio of splat to droplet diameter ($\xi = D_p/d_p$)
$\psi$      sphericity of a particle, Eq. 4.5 (m)
$\psi$      particle vaporization constant, Eq. 4.56 (m$^2$/s)

## References

Amouroux, J., A. Gicquel, S. Cavadias, D. Morvan, and F. Arefi. 1985. Progress in the applications of plasma surface modifications and correlations with the chemical properties of the plasma phase. *Pure and Applied Chemistry* 57 (9): 1207–1222.

Arnauld, Ph., S. Cavadias, and J. Amouroux. 1985. *The interaction of a fluidized bed with a thermal plasma. Application to limestone decomposition, ISPC-7*, ed. Timmermans, 1195–1200. Eindhoven: University of Technology of Eindhoven.

Asaki, Z., Y. Fakunaka, T. Nagasi, and Y. Kondo. 1974. Thermal decomposition of limestone in a fluidized bed. *Metallurgical Transactions* B-5: 381–390.

Bach, Fr.W., Z. Babiak, T. Duda, T. Rothardt, and G. Tegeder. 2001. *Impact of self propagating high temperature synthesis of spraying materials on coatings based on aluminum and metal-oxides, ITSC-2001: New surfaces for a new millennium*, ed. C.C. Berndt, K.A. Khor and E.F. Lugsheider, 497–502. Materials Park: ASM International.

Borgianni, C., M. Capitelli, F. Cramarossa, L. Triolo, and L. Molinari. 1969. The behavior of metal oxides injected into an argon induction plasma. *Combustion and Flame* 13: 181–194.

Borisov, Y., and A. Borisova. 1993. *Application of self-propagating high-temperature synthesis in thermal spraying technology, ITSC-1993: Research, design and applications*, ed. T.F. Bernicki (pub.), 139–144. Materials Park: ASM International.

Borisov, Yu.S., A.L. Borisova and L.K. Shvedova. 1986. Transition metal-nonmetallic refractory compound composite powders for thermal spraying. *Advances in Thermal Spraying*: 323–329. Pergamum Press.

Boulos, M.I. 1976. Flow temperature field in the fire ball of an inductively coupled plasma. *IEEE Transactions on Plasma Science* PS-4: 28–39.

———. 1978. Heating of powders in the fire ball of an induction plasma. *IEEE Transactions on Plasma Science* PS-6 (2): 93–106.

———. 1985. The inductively coupled R.F. Plasma. *Journal of Pure and Applied Chemistry* 57: 1321–1352.

———. 1992. RF induction plasma spraying: State-of-the-art review. *Journal of Thermal Spray Technology* 1 (1): 33–40.

———. 2003. Spheroidization and densification of powders. In *Continuing education course on Thermal Plasmas, held in conjunction with ISPC-16*, ed. P. Fauchais. University of Limoges.

———. 2004. Plasma interaction with a dispersed medium Ch 6.2. In *Continuing education course in conjunction with ITSC-2004*, ed. J. Heberlein. Minneapolis: University of Minnesota.

———. 2016. The role of transport phenomena and modelling in the development of thermal plasma technology. *Journal of Plasma Chemistry Plasma Processing* 36: 3–29.

Boulos, M.I., and D.C.T. Pei. 1969. Simultaneous heat and mass transfer from a single sphere to a turbulent air stream. *Canadian Journal of Chemical Engineering* 47: 30–34.

Boulos, M.I., P. Fauchais, A. Vardelle, and E. Pfender. 1993. Fundamentals of plasma particle momentum and heat transfer. In *Plasma spraying theory and applications*, ed. R. Suryanarayanan. World Scientific Singapore.

Boulos, M., P. Fauchais, and E. Pfender. 1994. *Thermal plasmas fundamental and applications*. Plenum Press, NY, 452 pages.

Bouneder, M. 2006. *Modelling of heat and mass transfer within composite metal/ceramic particles in DC plasma spraying*. PhD thesis University of Limoges, France.

Bouneder, M., M. El Ganaoui, B. Pateyron, and P. Fauchais. 2003. Thermal modeling of composite iron/alumina particles sprayed under plasma conditions Part I: Pure conduction. *High Temperature Material Processes* 7 (4): 547–555.

Bourdin, E., M.I. Boulos, and P. Fauchais. 1983. Transient conduction to a single sphere under plasma conditions. *International Journal of Heat and Mass Transfer* 26: 567–579.

Bouyer, E., F. Gitzhoffer, and M.I. Boulos. 1997a. Experimental study of suspension plasma spraying of hydroxyapatite. In *Progress in plasma processing of materials*, ed. P. Fauchais, 735–750. Begell House.

Bouyer, E., M. Müller, N. Dard, F. Gitzhofer, and M.I. Boulos. 1997b. Suspension plasma spraying for powder preparation. In *Progress in plasma processing of materials*, ed. P. Fauchais, 751–759. Begell House.

Bouyer, E., F. Gitzhofer, and M.I. Boulos. 1997c. The suspension plasma spraying of bioceramics by induction plasma. *JOM* 49 (2): 58–68.

Bouyer, E., D.W. Branston, G. Lins, M. Müller, J. Verleger, and M. Von Bradke. 2001. Deposition of yttria-stabilized zirconia coatings using liquid precursors. In *Progress in plasma processing of materials*, ed. P. Fauchais, 501–506. Begell House.

Bouyer, L., X. Ma, A. Ozturk, E.H. Jordan, N.P. Padture, B.M. Cetegen, D.T. Xiao, and M. Gell. 2004. Processing parameter effects on solution precursor plasma spray process spray patterns. *Surface Coating Technology* 183 (1): 51–61.

Chang, P., and K.A. Khor. 1996. Influence of powder characteristics on plasma sprayed hydroxyapatite coatings. *Journal of Thermal Spray Technology* 5 (3): 310–316.

Chen, Xi. 1988. Particle heating in a thermal plasma. *Pure and Applied Chemistry* 60: 651–662.

Chen, Xi, and Xioming Chen. 1989. Drag on a metallic or non-metallic particle exposed to a rarefied plasma flow. *Plasma Chemistry and Plasma Processing* 9 (3): 387–408.

Chen, Xi, and He Ping. 1986. Heat transfer from a rarefied plasma flow to a metallic or nonmetallic particle. *Plasma Chemistry and Plasma Processing* 6 (4): 313–333.

Chen, Xi, and E. Pfender. 1982a. Unsteady heating and radiation effects of small particles in a thermal plasma. *Plasma Chemistry and Plasma Processing* 2: 293–316.

———. 1982b. Heat transfer to a single particle exposed to a thermal plasma. *Plasma Chemistry and Plasma Processing* 2 (2): 185–212.

———. 1983a. Effect of the Knudsen number on heat transfer to a particle immersed into a thermal plasma. *Plasma Chemistry and Plasma Processing* 39: 7–113.

———. 1983b. Behavior of small particles in a thermal plasma flow. *Plasma Chemistry and Plasma Processing* 3: 351–366.

Chen, Xi, Y.P. Chyou, Y.C. Lee, and E. Pfender. 1985. Heat transfer to a particle under plasma conditions with vapor contamination from the particle. *Plasma Chemistry and Plasma Processing* 5 (2): 119–141.

Chen, K., and M.I. Boulos. 1994. Turbulence in induction plasma modelling. *Journal of Physics D: Applied Physics* 27: 946–952.

Chyou, Y.P., and E. Pfender. 1989. Behavior of particulates in thermal plasma flows. *Plasma Chemistry and Plasma Processing* 9 (1): 45–71.

Cliche, G., and S. Dallaire. 1991. Synthesis and deposition of TiC-Fe coatings by plasma spraying. *Surface and Coating Technology* 46: 199–206.

Clift, R., J.R. Grace, and J.E. Weber. 1978. *Bubbles, drops and particles*. Academic.

Cram, L. 1985. Statistical evaluation of radiative power losses from thermal plasmas due to spectral lines. *Journal of Physics D: Applied Physics* 18: 401–411.

Dai S., J.-P. Delplanque, R.H. Rangel, and E.J. Lavernia. 1998. *Modeling of reactive spray atomization and deposition, NTSC-1998: Meeting the challenges of the 21st century,* ed. C. Coddet (pub.), Vol. 1, 341–346. Materials Park: ASM International.

Dallaire, S. 1992. Thermal spraying of reactive materials to form wear-resistant composite coatings. *Journal of Thermal Spray Technology* 1 (1): 41–47.

Dallaire, S., and B. Champagne. 1984. Plasma spray synthesis of TiB2-Fe coatings. *Thin Solid Films* 118: 477–483.

Dallaire, S., and G. Cliche. 1992. The influence of composition and process parameters on the microstructure of TiC-Fe multiphase and multilayer coatings. *Surface and Coating Technology* 50: 233–239.

Deevi, S.C., V.K. Sikka, C.J. Swindeman, and R.D. Seals. 1997. Reactive spraying of nickel-aluminide coatings. *Journal of Thermal Spray Technology* 6 (3): 335–344.

Denoirjean, A., P. Lefort, and P. Fauchais. 2003. Nitridation process and mechanism of Ti-6Al-4V particles by plasma spraying. *Physical Chemistry Chemical Physics* 5: 5133–5138.

Diez, P., and R.W. Smith. 1993. The influence of powder agglomeration methods on plasma sprayed yttria coatings. *Journal of Thermal Spray Technology* 2 (2): 165–172.

Ducos, M. 1988. Rechargement par plasma a arc transferé (in French), In Arc plasma processes, Union Internationale de l'Electrothermie, DOPEE diffusion, Av. F. Roosevelt, 77210, Avon, France, 251–263 (in French).

Eckardt, T., W. Malleaer, and D. Stove. 1994. *Reactive plasma spraying of silicon in controlled nitrogen atmosphere, NTSC-1994: Industrial applications,* ed. C.C. Berndt and S. Sampath, 515–520. Materials Park: ASM International.

Espié, G., P. Fauchais, B. Hannoyer, J.C. Labbe, and A. Vardelle. 1999. Effect of metal particles oxidation during the APS on the wettability. In *Heat and mass transfer under plasma condition*, ed. P. Fauchais, J. Van der Mullen, and J. Heberlein, vol. 891, 143–151. Annals of NY Academy of Sciences.

Espié, G., P. Fauchais, J.C. Labbe, A. Vardelle, and B. Hannoyer. 2001. *Oxidation of iron particles during APS, ITSC-2001: New surface for a new Millenium*, ed. C.C. Berndt, K.A. Khor and E. Lugscheider, 821–828. Materials Park: ASM International.

Espie, G., A. Denoirjean, P. Fauchais, J.C. Labbe, J. Dudsky, O. Scheeweiss, and K. Volenik. 2005. In flight oxidation of iron particles sprayed using gas and water stabilized plasma torches. *Surface and Coatings Technology* 195: 17–28.

Essoltani, A., P. Proulx, M.I. Boulos, and A. Gleizes. 1990. Radiation and self-absorption in argon - Iron plasmas at atmospheric pressure. *Journal of Analytical Atomic spectrometry* 5: 543–547.

———. 1991. *Radiative effects on plasma-particle heat transfer in the presence of metallic vapors, ISPC-10*, ed. U. Ehlemann et al. University of BOCHUM, Germany.

———. 1993. A combined convective, conductive and radiative heat transfer study for an evaporating metallic particle under plasma conditions. *High Temperature Materials and Processes* 2: 37–46.

———. 1994. Effect of the presence of iron vapors on the volumetric emission of Ar/Fe and Ar/Fe/$H_2$ plasmas. *Plasma Chemistry Plasma processing* 14 (3): 301–315.

Fan, X., and T. Ishigaki 1998. *Fabrication of composite SiC-MoSi2 powders through plasma reaction process, NTSC-1998: Meeting the challenges of the 21st century,* ed. C. Coddet, Vol. 2, 1161–1166. Materials Park: ASM International.

Fauchais, P. 2004. Understanding plasma spraying. *Journal of Physics D: Applied Physics* 37: 86–108.

Fauchais, P., and G. Montavon. 2010. Latest developments in suspension and liquid precursor thermal spraying. *Journal of Thermal Spray Technology* 19: 226–239.

Fauchais, P., J.F. Coudert, and M. Vardelle. 1989. *Diagnostics in thermal plasma processing, plasma diagnostics*, ed. O. Ociello and D.L. Flamm, Vol. 1, 349–446. Academic.

Fauchais, P., A.C. Léger, M. Vardelle, and A. Vardelle. 1997a. Formation of plasma sprayed oxide coatings. In *Proceedings of the Julian Szekely Memorial symposium on materials processing*, ed. H.Y. Sohn, J.W. Evans, and D. Apelian, 571–582. T.M.S.

Fauchais, P., A. Vardelle, and A. Denoirjean. 1997b. Reactive thermal plasmas: Ultrafine particle synthesis and coating deposition. *Surface and Coatings Technology* 979: 66–78.

Fauchais, P., V. Rat, C. Delbos, J.F. Coudert, T. Chartier, and L. Bianchi. 2005a. Understanding of suspension dc plasma spraying of finely structured coating for SOFC. *IEEE Transactions on Plasma Science* 33: 920–930.

Fauchais, P., M. Vardelle, J.F. Coudert, A. Vardelle, C. Delbos, and J. Fazilleau. 2005b. Plasma spraying from thick to thin coatings and micro to nano structured coatings. *Pure and Applied Chemistry* 77: 475–485.

Fauchais, P., R. Etchart-Salas, C. Delbos, M. Tognovi, V. Rat, J.F. Coudert, and T. Chartier. 2007. Suspension and solution plasma spraying of finely structured coatings. *Journal of Physics D: Applied Physics* 40: 2394–2406.

Fauchais, P., R. Etchart-Salas, V. Rat, J.F. Coudert, N. Caron, and K. Wittmann. 2008. Parameters controlling liquid plasma spraying: Solutions, sols or suspensions. *Journal of Thermal Spray Technology* 17 (1): 31–59.

Fauchais, P., G. Montavon, R. Lima, and B. Marple 2011. Engineering a new class of thermal spray nano-based microstructures from agglomerated nanostructured particles, suspensions and solutions: An invited review. *Journal of Physics D: Applied Physics* 44: 093001 (53p).

Fauchais, P., A. Joulia, S. Goutier C. Chazelas, M. Vardelle, A. Vardelle, and S. Rossignol. 2013. Suspension and solution plasma spraying. *Journal of Physics D: Applied Physics* 46: 224015 (14pp).

Fauchais, P., J.V. Heberlein, and M.I. Boulos. 2014. *Thermal spray fundamentals, From powder to part*. Springer, 1550 pages.

Fauchais, P., M. Vardelle, A. Vardelle, and S. Goutier. 2015. What do we know, what are the current limitations of suspension plasma spraying? *Journal of Thermal Spray Technology* 24 (7): 1120–1129.

Fazilleau, J. 2003. *Contribution to the understanding of the phenomena implied in the achievement of finely structured oxide coatings by suspension plasma spraying*. PhD. Thesis, In French, University of Limoges, France.

FIDAP Code distributed by Fluent Inc., Lebanon, NH, USA.

Fizdon, J.K. 1979. Melting of powder grains in a plasma flame. *International Journal of Heat and Mass Transfer* 22: 749–761.

Fukanuma, H., N. Ohno, Bo Sun, and R. Huang. 2006. *The influence of particle morphology on in-flight particle velocity in cold spray, ITSC-2006*. Materials Park: ASM International.

Ganser, G.H. 1993. A rational approach to drag prediction of spherical and non-spherical particles. *Powder Technology* 77: 143–152.

Gell, M. 1995. Application opportunities for nanostructured materials and coatings. *Materials Science and Engineering* 204: 246–251.

Gell, M., E.H. Jordan, Y.H. Sohn, D. Goberman, L. Shaw, and T.D. Xiao. 2001. Development and implementation of plasma sprayed nanostructured ceramic coatings. *Surface and Coatings Technology* 146–147: 48–54.

El Hage, M., J. Mostaghimi, and M.I. Boulos. 1989. A turbulent flow model for the R.F. inductively coupled plasma. *Journal of Applied Physics* 65: 4178–4185.

Haller, B. 2006. *Study of a process combining plasma spraying and SHS: application to Ti-graphite mixtures*. PhD Thesis, University of Limoges, France (in French).

Haller, B., J.P. Bonnet, P. Fauchais, A. Grimaud, and J.C. Labbe. 2004. *TiC based coatings prepared by combining SHS and plasma spraying, ITSC-2004 Innovative Equipment and Process Technology* V (pub.). Düsseldorf: DVS.

He, P.-J., S. Yin, C. Song, F. Lapostolle, and H.-L. Liao. 2016. Characterization of Yttria-stabilized zirconia coatings deposited by low-pressure plasma spraying. *Journal of Thermal Spray Technology* 25 (3): 558–566.

Heberlein, J., J. Mentel, and E. Pfender. 2007. The anode region of electric arcs - A survey. *Journal of Physics D: Applied Physics* 43: 023001.

Humbert, P. 1991. *Development of pilot set-up for silicon purification by induction thermal plasma and modelling of mass and heat transfers plasma-particles*. Ph.D. Thesis, Univ. of Paris VI, ENSCP, Paris, France.

Hurevich, V., I. Smurnov, and L. Pawlowski. 2002. Theoretical study of the powder behavior of porous particles in a flame during plasma spraying. *Surface and Coatings Technology* 151–152: 370–376.

Jiang, X.L., F. Gitzhoffer, M.I. Boulos, and R. Tiwari. 1994. *Induction plasma reactive deposition of tungsten and titanium carbides, NTSC-1994: Industrial applications*, ed. C.C. Berndt and S. Sampath (pub.), 451–456. Materials Park: ASM International.

Laha, T., K. Balani, A. Agarwal, S. Patil, and S. Seal. 2005. Synthesis of nanostructured spherical aluminum oxide powders by plasma engineering. *Metallurgical and Materials Transactions A* 36A (2005): 301–309.

Lapple, C.E., and C.B. Shepherd. 1940. Calculation of particle trajectories. *Industrial and Engineering Chemistry* 32 (5): 605–617.

Lee, C.S., and R.D. Reitz. 2001. Effect of liquid properties on the break-up mechanism of high-speed liquid drops. *Atomization and Sprays* 11: 1–18.

Lee, Y.C., C. Hsu, and E. Pfender. 1981. *Modelling of particle injection into a DC plasma jet ISPC-5*. Vol. 2, 795–801. Edinburgh.

Lee, Y.C., Y.P. Chyou, and E. Pfender. 1985. Particle dynamics and particle heat and mass transfer in thermal plasmas. Part II. Particle heat and mass transfer in thermal plasmas. *Plasma Chemistry and Plasma Processing* 5 (4): 391–414.

———. 1997. Particle dynamics and particle heat and mass transfer in thermal plasmas. Part III. Thermal plasma jet reactors and multi-particle injection. *Plasma Chemistry and Plasma Processing* 7 (1): 1–27.

Lefebvre, A.H. 1989. *Atomization and sprays*. Hemisphere Publishing Corp.

Legoux, J.G., and S. Dallaire. 1993. Copper-TiB$_2$ coatings by plasma spraying reactive micropellets. In *Proc. NTSC-1993*, ed. C.C. Berndt, 429–432. Materials Park: ASM International.

Lewis, J.W., and W.H. Gauvin. 1973. Motion of particles entrained in a plasma jet. *AICHE Journal* 19 (6): 982–990.

Li, K.-I., M. Vardelle, A. Vardelle, P. Fauchais, and C. Trassy. 1995. Comparisons between single and double flow injectors in the plasma spraying process, NTSC-1005.

Lima, R.S., and B.R. Marple. 2007. B thermal spray coatings engineered from nano-structured ceramic agglomerated powders for structural, thermal barrier and biomedical applications: A review. *Journal of Thermal Spray Technology* 16: 40–63.

———. 2008. Nanostructured YSZ thermal barrier coatings engineered to counteract sintering effects. *Materials Science and Engineering A* 485: 182–193.

Marchand, C., C. Chazelas, G. Mariaux, and A. Vardelle. 2007. *Liquid precursor plasma spraying: Modelling the interaction between the transient plasma jet and the droplets, ITSC-2007: Global coating solutions*, ed. B R Marple et al., 196–201. Materials Park: ASM International.

Marchand, C., A. Vardelle, G. Mariaux, and P. Lefort. 2008. Modelling of the plasma spray process with liquid feedstock injection. *Surface and Coating Technology* 202: 4458–4464.

Marchand, O., L. Girardot, M.P. Planche, P. Bertrand, Y. Bailly, and G. Bertrand. 2011. An insight into suspension plasma spray: Injection of the suspension and its interaction with the plasma flow. *Journal of Thermal Spray Technology* 20 (6): 1310–1320.

Mostaghimi, J., and E. Pfender. 1984. Effects of metallic vapor on the properties of an argon arc plasma. *Plasma Chemistry Plasma Processing* 4 (2): 129–139.

Mostaghimi, J., P. Proulx, and M.I.A. Boulos. 1987. Two-temperature model of the inductively coupled R.F. Plasma. *Journal of Applied Physics* 61 (5): 1753–1760.

Mostaghimi, J., and M.I. Boulos. 1989. Two-dimensional electromagnetic field effects in R.F. inductively coupled plasmas. *Journal of Plasma Chemistry and Plasma Processing* 9: 23–42.

Mostaghimi, J., P. Proulx, M.I. Boulos, and R.M. Barnes. 1985. Computer modeling of the emission patterns for a spectrochemical ICP. *Spectro-chemical Acta* 40B: 153–166.

Murray, W.D., and F. Landis. 1959. Numerical and machine solutions of transient heat-conduction problems involving melting or freezing-Part I. Method of analysis and sample solutions. *Journal of Heat Transfer* 81: 106112.

Neiser, R.A., M.F. Smith, and R.C. Dykhuisen. 1998. Oxidation in wire HVOF-sprayed steel. *Journal of Thermal Spray Technology* 7 (4): 537–545.

Oberkampf, W.L., and M. Talpallikar. 1994. Analysis of a high velocity oxygen-fuel (HVOF) thermal spray torch, part 1: Numerical formulation. In *Thermal spray industrial applications*, ed. C.C. Berndt and S. Sampath, 381–386. ASM International, Materials Park.

Pfender, E. 1985. Heat and momentum transfer to particles in thermal plasma flows. *Pure and Applied Chemistry* 57: 1179–1196.

———. 1989. Particle behavior in thermal plasmas. *Plasma Chemistry and Plasma Processing* 9 (1): 167S–194S.

———. 1999. Thermal plasma technology: Where do we stand and where are we going? *Plasma Chemistry and Plasma Processing* 19 (1): 1–31.

Pfender, E., and C.H. Chang. 1998. *Plasma spray jets and plasma-particulate interaction: Modeling and experiments, ITSC-1998: Meeting the challenges of 21st century*, ed. C. Coddet, Vol. 1, 315–328. Materials Park: ASM International.

Pfender, E., and Y.C. Lee. 1985. Particle dynamics and particle heat and mass transfer in thermal plasmas. Part I. The motion of a single particle without thermal effects. *Plasma Chemistry Plasma Processing* 5 (3): 211–237.

Ponticaud, C., A. Grimaud, A. Denoirjean, P. Lefort, and P. Fauchais. 2001. Titanium powder nitridation by reactive plasma spraying. In *Progress in plasma processing of materials*, ed. P. Fauchais, J. Amouroux, and M.F. Elchinger, 527–536. Begell House Inc.

Proulx, P., J. Mostaghimi, and M.I. Boulos. 1985a. Plasma-particle interaction effects in induction plasma modelling under dense loading conditions. *International Journal of Heat and Mass Transfer* 28: 1327–1336.

———. 1987a. Heating of powders in an R.F. inductively coupled plasma under dense loading conditions. *Plasma Chemistry and Plasma Processing* 7 (1): 29–53.

———. 1990a. Loading and radiation effects in plasma jet modelling. *Journal de Physique Colloques* 51 (C5): 263–270.

———. 1991a. Modelling of the vaporization of small metallic particles in a D.C. plasma jet. *Heat Transfer in Thermal Plasma Processing* 161: 155–160.

———. 1991b. Radiative effects in ICP modelling. *International Journal of Heat and Mass Transfer* 31 (10): 2571–2579.

Reist, P.C. 1993. *Aerosol science and technology*. New York: McGraw Hill.

Rudinger, G. 1980. Fundamentals of gas-particle flow. In *Handbook of powder technology*, ed. J.C. Williams and T. Allen, vol. 2. Amsterdam: Elsevier.

Sayegh, N.N., and W.H. Gauvin. 1979. Analysis of variable property heat transfer to a single sphere in high temperature surrounding. *AICHE Journal* 25: 522–534.

Schwier, C. 1986. *Plasma spray powders for thermal barrier coating. Advance thermal spray*, 277–286. Pergamon Press.

———. 2005. In-flight oxidation of stainless steel in plasma spraying. *Journal of Thermal Spray Technology* 14 (1): 177–124.

Shaw, K.G., K.P. McCoy, and J.A. Trogolo. 1994. *Fabrication of composite spray powders using reaction systems, NTSC-1994: Industrial applications*, ed. C.C. Berndt and S. Sampath, 509–514. Materials Park: ASM International.

Smith, R.W., and Z.Z. Matasin. 1992. Reactive plasma spraying of wear-resistant coatings. *Journal of Thermal Spray Technology* 1 (1): 57–63.

Soo, S.L. 1967. *Fluid dynamics of multiphase systems*. New York: Blaisdell.

Taneda, S. 1956. Flow past a sphere. *Journal of the Physical Society of Japan* 11 (10): 1104.

Tsunekawa, Y., I. Ozdemir, and M. Okumiya. 2006. Plasma Sprayed Cast Iron Coatings Containing Solid Lubricant Graphite and h-BN Structure. *Journal of Thermal Spray Technology* 15 (2): 239–245.

Uglov, A.A., and A.G. Gnedovets. 1991. Effect of particle charging on momentum and heat transfer from rarefied plasma flow. *Plasma Chemistry Plasma processing* 11 (2): 251–267.

Vardelle, M., A. Vardelle, P. Fauchais, and M.I. Boulos. 1983. Plasma-particle momentum and heat transfer, modelling and measurements. *AIChE Journal* 29: 236–243.

———. 1988a. Particle dynamics and heat transfer under plasma conditions. *AIChE Journal* 34 (4): 567–573.

Vardelle, M., A. Vardelle, A. Denoirjean, and P. Fauchais. 1990. Heat treatment of zirconia powders with different morphologies under thermal spray conditions. In *MRS Spring meeting proceedings*, ed. D. Apelian and J. Szekely, vol. 190, 175–183. MRS.

Vardelle, A., M. Vardelle, P. Fauchais, P. Proulx, and M.I. Boulos. 1992 *Loading effect by oxide powders in DC plasma jets, NTSC-1992: International advances in coatings technology*, ed. C.C. Berndt, 543–548. Materials Park: ASM International.

Vardelle, M., A. Vardelle, K.-I. Li, P. Fauchais, and N.J. Themelis. 1996. Coating generation: Vaporization of particles in plasma spraying and splat formation. *Pure and Applied Chemistry* 68 (5): 1093–1099.

Vardelle, A., N.J. Themelis, B. Dussoubs, M. Vardelle, and P. Fauchais. 1997a. Transport phenomena in thermal plasmas. *Journal of High Temperature Material Processes* 1 (3): 295–317.

Vardelle, A., P. Fauchais, and P. Fauchais. 1997b. *Vaporization and ultra-fine particle generation during the plasma spraying processNTSC-1997: A United Forum for scientific and technological advances*, ed. C.C. Berndt, 543–548. Materials Park: ASM International.

Vardelle, A., P. Fauchais, B. Dussoubs, and N.J. Themelis. 1998. Heat generation and particle injection in a thermal plasma torch. *Plasma Chemistry and Plasma Processing* 18 (4): 551–574.

Vardelle, M., A. Vardelle, P. Fauchais, K.-I. Li, B. Dussoubs, and N.J. Themelis. 2001. Controlling particle injection in plasma spraying. *Journal of Thermal Spray Technology* 10 (2): 267–284.

Vardelle, A., M. Vardelle, H. Zhang, N.J. Themelis, and K. Gross. 2002. Controlling particle injection in plasma spraying. *Journal of Thermal Spray Technology* 11 (2): 244–284.

Volenik, K., J. Leitner, F. Hanousek, J. Dubsky, and B. Kolman. 1997. Oxides in plasma-sprayed chromium steel. *Journal of Thermal Spray Technology* 6 (3): 327–334.

Volenik, K., P. Chraska, J. Dubsky, J. Had, J. Leitner, and O. Schneewein. 2003. Oxidation of Ni-based alloys sprayed by a water-stabilized plasma gun (WSP). In *Thermal Spray-2003; Advancing the science and applying the technology*, ed. C. Moreau and B. Marple, 1033–1041. Materials Park: ASM Int.

White, F.M. 1974. *Viscous fluid flow*. McGraw Hill.

Xi, Chen, and E. Pfender. 1982a. Unsteady heating and radiation effects of small particles in a thermal plasma. *Plasma Chemistry and Plasma Processing* 2: 293–316.

———. 1982b. Heat transfer to a single particle exposed to a thermal plasma. *Plasma Chemistry and Plasma Processing* 2 (2): 185–212.

Xue, S., P. Proulx, M.I. Boulos. 2001. Extended − field electromagnetic model for the inductively coupled plasma. *Journal of Physics D: Applied Physics* 34: 1897−1906.

Xue, S., and M.I. Boulos. 2019a. Transient heating and evaporation of metallic particles under plasma conditions. *Journal of Physics D: Applied Physics* 52: 454002. (12 pages).

Xu, D.-Y., X.-C. Wu, and Chen Xi. 2002. Motion and heating of non-spherical particles in a plasma jet. *Surface and Coatings Technology* 171 (1–3): 149–156.

Ye, R., P. Proulx, and M.I. Boulos. 2000. Particle turbulent dispersion and loading effects in an inductively coupled radio frequency plasma. *Journal of Physics D: Applied Physics* 33: 2154–2162.